CHAPTER 4

Mesogenic Schiff's base derived from thiadiazole moiety

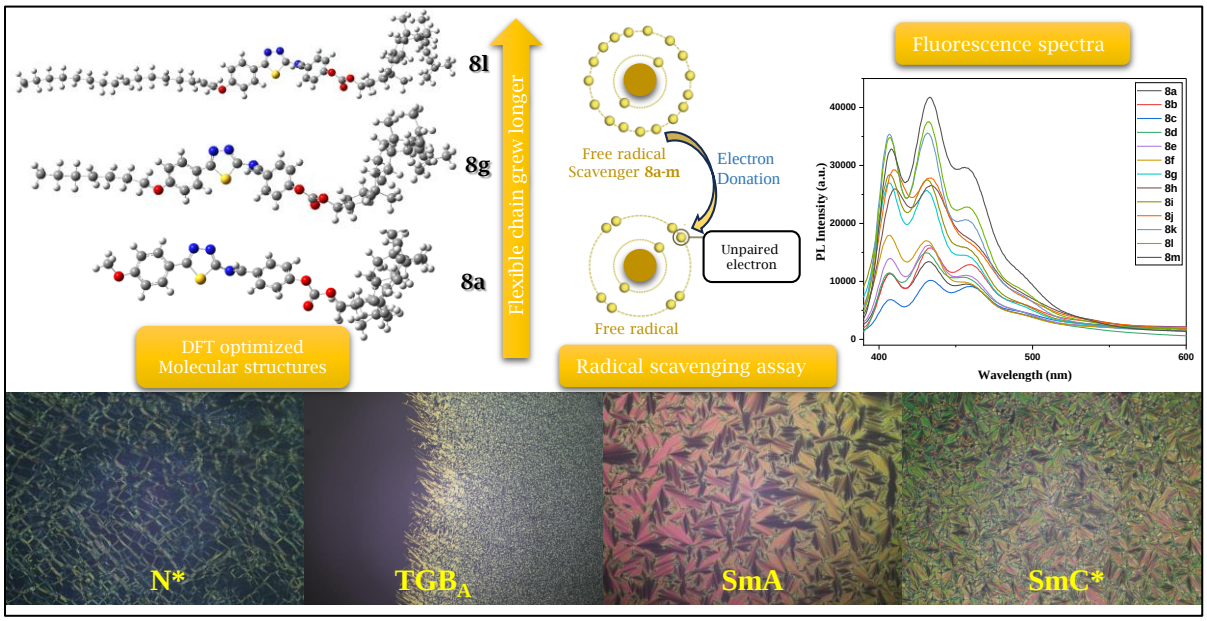

4.1. Introduction

Cholesterol, a natural sterol molecule, is an essential component of cell membranes and is required for preserving their fluidity and integrity [1]. The ability of cholesterol and its derivatives to form liquid crystalline phases has been widely investigated. Along with improving stability and self-assembly behaviour, adding cholesterol to liquid crystal systems also offers unique features coming from the cholesterol moiety. Cholesterol-based liquid crystals offer several advantages over conventional liquid crystals, including enhanced mesophase stability due to the rigid and steroidal structure of cholesterol, allowing the development of well-defined LC phases over a varied thermal span and also the stronger intermolecular interactions that lead to improved ordering and phase transition characteristics [2]. Depending on the structure of the steroidal skeleton and the substituents attached, they can form a wide variety of liquid crystalline phases, including frustrated phases [3,4]. Typically, frustration of phases occurs predominantly in chiral systems with substantial enantiomeric excess and strong molecular chirality, especially with a short pitch. Despite the extensive reporting of at least 3000 conventional monomeric LCs incorporating a cholesterol moiety as the chiral component, only a limited subset of mesogens derived from cholesterol exhibit the TGB_A or related phases [5–8].

The significance of heterocycles as core elements in LCs lies in its ability to introduce lateral and/or longitudinal dipoles and induce variations in the structural constituent. These constituents grasp huge probability for use in angular light regulation and organic photovoltaics (OPVs) [9], all optical signal processing, optical information storage [10], charge transport and energy transfer material [11], OTF transistors [12,13], fast switching ferroelectric material [14], fluorophores for detecting and analysing biomolecule [15], organic light-emitting diodes (OLEDs) [16,17] etc..

Due to their excellent thermal and chemical stability, electron deficiency, good electron-accepting ability, and photoluminescent properties, mesogens incorporating sulphur-nitrogen heterocycles, such as the 1,3,4-thiadiazole ring, have been studied as excellent candidates for material applications. Though the number of structural adjustments researched is very narrow, 1,3,4-thiadiazoles are comparatively common in previous works. In most systems, aryl components or a combination of aryl as well as alkyl/cyclo alkyl components are substituted at the 2- and 5-positions of the 1,3,4-thiadiazole core [18–22]. Therefore, depending on the most recent developments in the area, the specific properties and uses of thiadiazole-based liquid crystals may change.

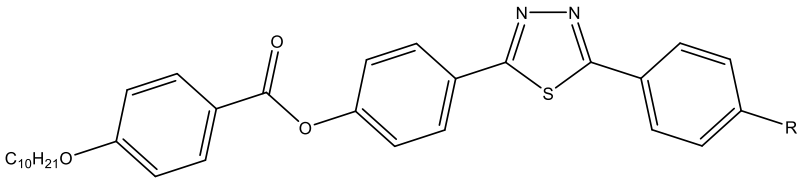

(a) Monomer

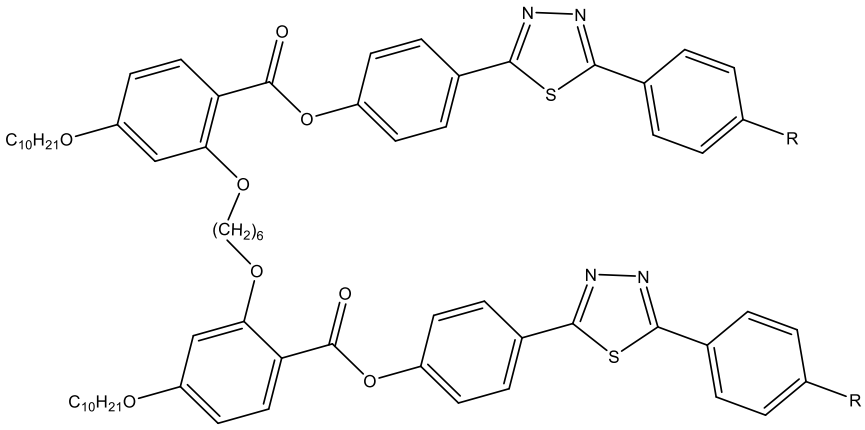

(b) H-shaped dimer

where R = OCH_3 and F

Figure 4.1 (a and **b):** Molecular structure mono and H-shaped dimer

When Dimitrowa et al. [23] published a set of 1,3,4-thiadiazoles in 1980, they provided one of the earliest instances of mesogenic 1,3,4-thiadiazoles. Jie Han et.al. [24] **(Figure 4.1 (a** and **b))**, have synthesized two H-shaped LC 1,3,4-thiadiazole dimers and their analogous monomers dimers, where the dimers exhibited an enantiotropic / monotropic N mesophases, while the monomers displayed enantiotropic N and/or SmA phases. The H-shaped dimers had significantly lower clearing temperatures compared to the analogous rod-like monomers.

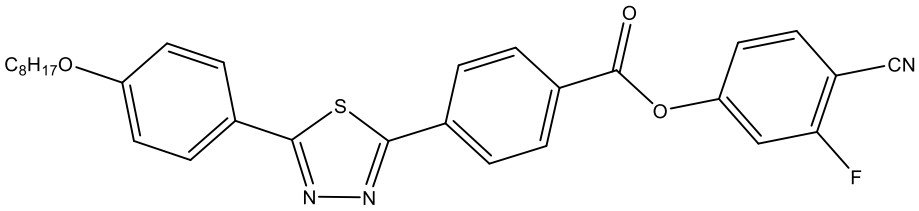

(c)

Figure 4.1 (c): Molecular structure of LC with 3-fluoro-4-cyanophenyloxy group

New series of LC compounds containing 1,3,4-oxa/thiadiazoles terminal 3-fluoro-4-cyanophenyloxy group have been synthesized by Wen-Yue Zhong et.al. [25] **(Figure 4.1 (c))**, where thiadiazole analogues exhibited SmA and SmC phases throughout a broad temperature range, whereas oxadiazoles only showed a N phase.

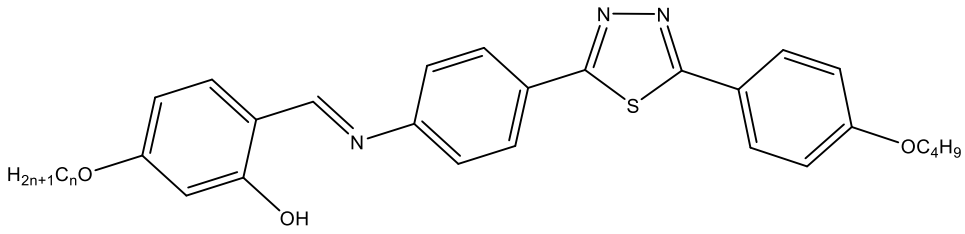

(d)

where n = 4,8,10,12,14,16,18

Figure 4.1 (d): Molecular structure of hockey sticks shaped LC

S K Saha et.al. [26] **(Figure 4.1 (d))**, hockey stick like liquid crystals containing 2,5-diphenyl-thiadiazole, where the higher homologues predominantly displayed SmC and SmA mesophases. Many calamitic, bent core, hockey stick shaped, star shaped, di, tetra as well as polycatenars, etc. thiadiazole based derivatives have been reported showing various typed of mesophases as well [19,27–30].

Also, many cholesterol-based monomers, dimers, trimers, tetramers as well as polymers have been synthesized exhibiting broad types of phases including twist grain boundary phases [31–40]. Additionally, cholesterol-based mesogenic compounds containing heterocyclic moiety have also been reported but to a limited extent.

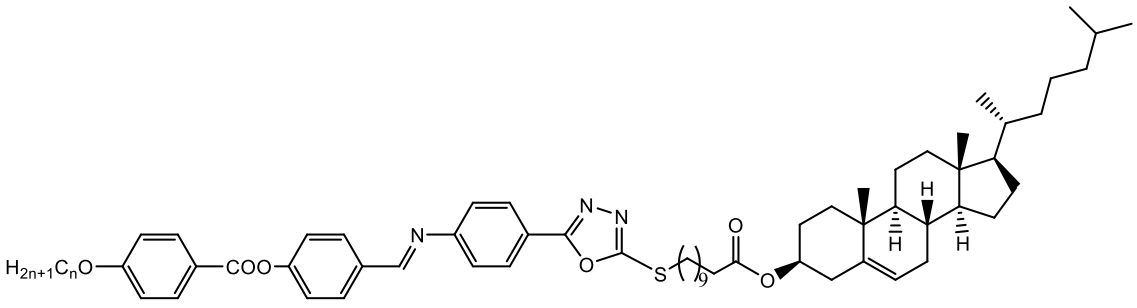

where n = 10,12,14,16,18

(e)

Figure 4.1 (e): Molecular structure of LC dimer with cholesterol and oxadiazole moiety

K. C. Majumdar et.al. [41] **(Figure 4.1 (e))**, synthesized cholesterol-based LC dimer with oxadiazole moiety exhibiting very infrequent broad temperature range, completely enantiotropic twist grain boundary TGB_C* phases where the phase was very much dependent on the terminal alkyl chain.

Following this, a variety of chiral dimers were also prepared by B. Pradhan et al. [42] by linking mesogenic cholesterol cores to bent structures of 1,3,4-thiadiazole **(Figure 4.1 (f))**, 1,3,4-oxadiazole **(Figure 4.1 (g))**, or 1,2,4-oxadiazole substitutes. Results indicated that, 1,3,4-oxadiazole core stabilizes frustrated phases such as TGB_A, TGB_C*, BPs and also re-entrant TGB_A, as well as SmA and SmC* phases, while the regioisomeric core exhibits only smectic

phases. The bending angle of the central core of the achiral unit is crucial for anchoring frustrated phases. Chiral dimers containing 1,3,4-thiadiazole showed a N* and/or BP phase, and SmA mesophase.

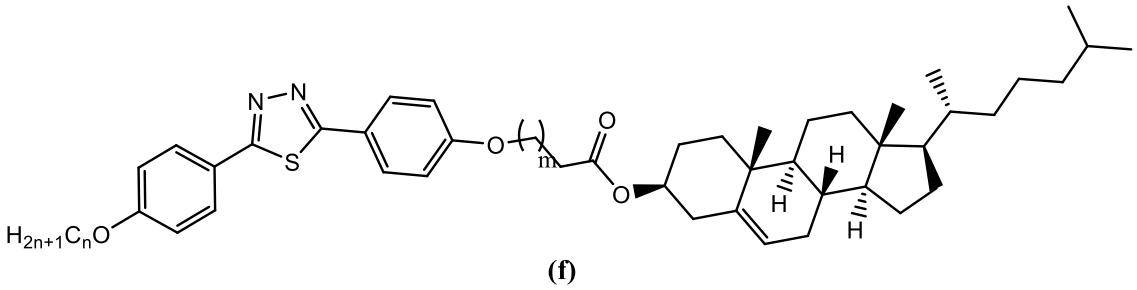

(f)

where n = 3,4,5,7
m = 8

Figure 4.1 (f): Molecular structure of LC dimer containing thiadiazole

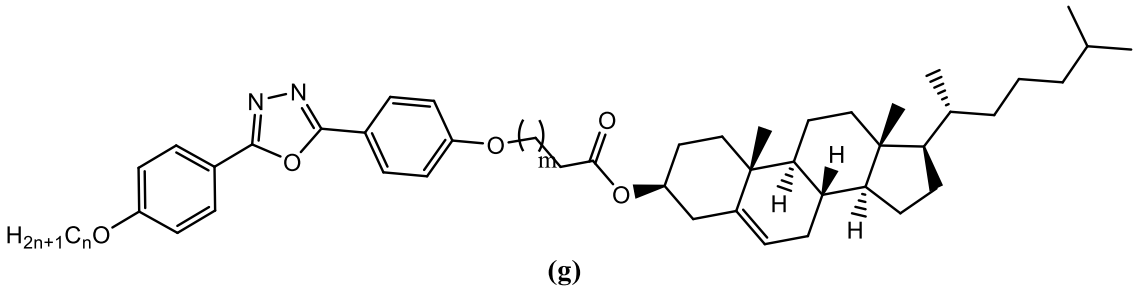

(g)

where n = 3,4,5,7
m = 8,9,10

Figure 4.1 (g): Molecular structure of LC dimer containing oxadiazole

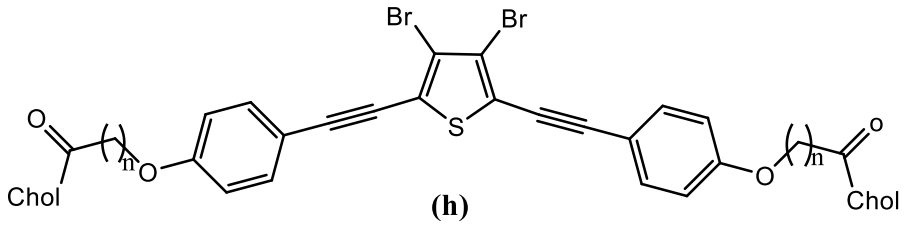

(h)

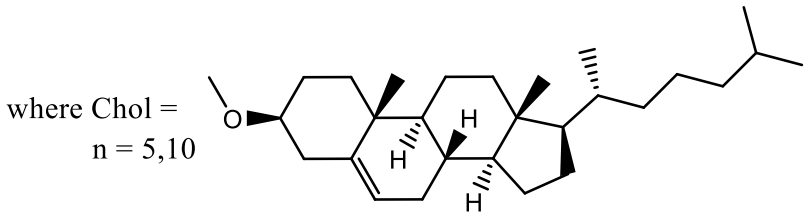

Figure 4.1 (h): Molecular structure of thiophene linked cholesteryl LC

K. C. Majumdar et.al. [43] **(Figure 4.1 (h))**, also reported thiophene linked cholesteryl liquid crystalline compound exhibit SmA and N* phase transitions. His group also reported [44] **(Figure 4.1 (i))** cholesterol-based LC with phenyl thiophene unit containing Schiff's base linkages, which exhibited N*, SmA, SmC* and TGB phases.

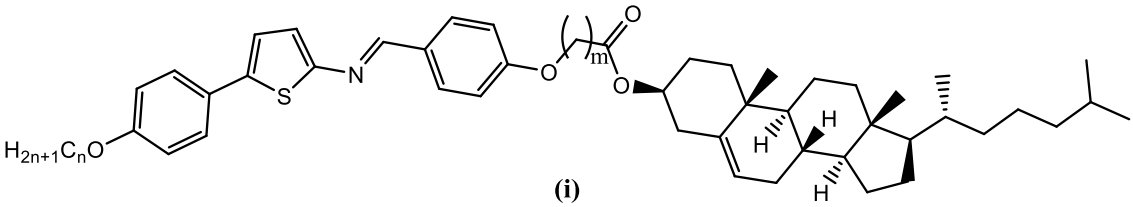

(i)

where m = 5,10
n = 6,8,12

Figure 4.1 (i): Molecular structure of LC with thiophene and cholesterol unit

In consideration of these findings, we present the synthesis of a novel class of liquid crystalline material, accompanied by comprehensive characterization and evaluation of its thermal, photophysical properties, and radical scavenging activity. This investigation focuses on a series of luminescent cholesterol-based Schiff's base derivatives incorporating a thiadiazole moiety.

4.2. Experimental

4.2.1. Materials

Cholesteryl chloroformate was purchased from Sigma-Aldrich Chemicals, USA. 1,1-diphenyl-2-picrylhydrazyl (for antioxidant assay) was purchased from TCI Chemicals, Japan. 4-Hydroxy benzoic acid, 4-hydroxy benzaldehyde, n-alkyl halides, thiosemicarbazide, potassium hydroxide, pyridine, glacial acetic acid and other reagents were purchased from Loba Chemie Pvt. Ltd., India. Tetrahydrofuran (THF), methanol and ethanol underwent drying treatment with standard methods. All remaining solvents and reagents were of AR grade and used without additional purification.

4.2.2. Techniques and measurements

The compounds' structures were established using standard spectroscopic techniques. Thin-layer chromatography (TLC) was performed on silica gel plates (Merck). FT-IR spectra were recorded on a Bruker spectrometer as KBr pellets. ^{1}H NMR and ^{13}C NMR spectral data were recorded on an Avance Bruker 400 spectrometer (400 MHz) with deuterated chloroform ($CDCl_3$) as solvent and TMS as an internal standard. The polarised optical microscopy (POM) study was observed with a Nikon Eclipse Ci-Pol microscope equipped with a Linkam (Linkam, Surrey, England) heating stage. Phase transition temperatures and thermodynamic parameters were determined by using differential scanning calorimetry (DSC-822, Mettler Toledo, with Stare software). The heating as well as cooling rates were 10°C/min. Indium was utilized as a

standard for calibrating the instrument. The thermal stability of the compounds was recorded using a thermogravimetry analyser (TGA-50, Shimadzu, Japan) with 3-7 mg of the sample in a platinum pan at a heating rate of 10°C/min. Thermo Finnigan's (Flash 1112 series EA) CHN analyser was used to carry out elemental analyses. Absorbance was recorded using a Shimadzu UV-1800 spectrophotometer (Japan). Photoluminescence and quantum yields (Φ_{PL}) were measured using a Shimadzu RF 6000 Spectro fluorophotometer (Japan). Gaussian 09, revision A.02 software was utilized for DFT calculations.

4.2.3. Synthesis and characterisation

Scheme 4.1 depicts the synthetic pathways for final Schiff's bases **8a-m.**

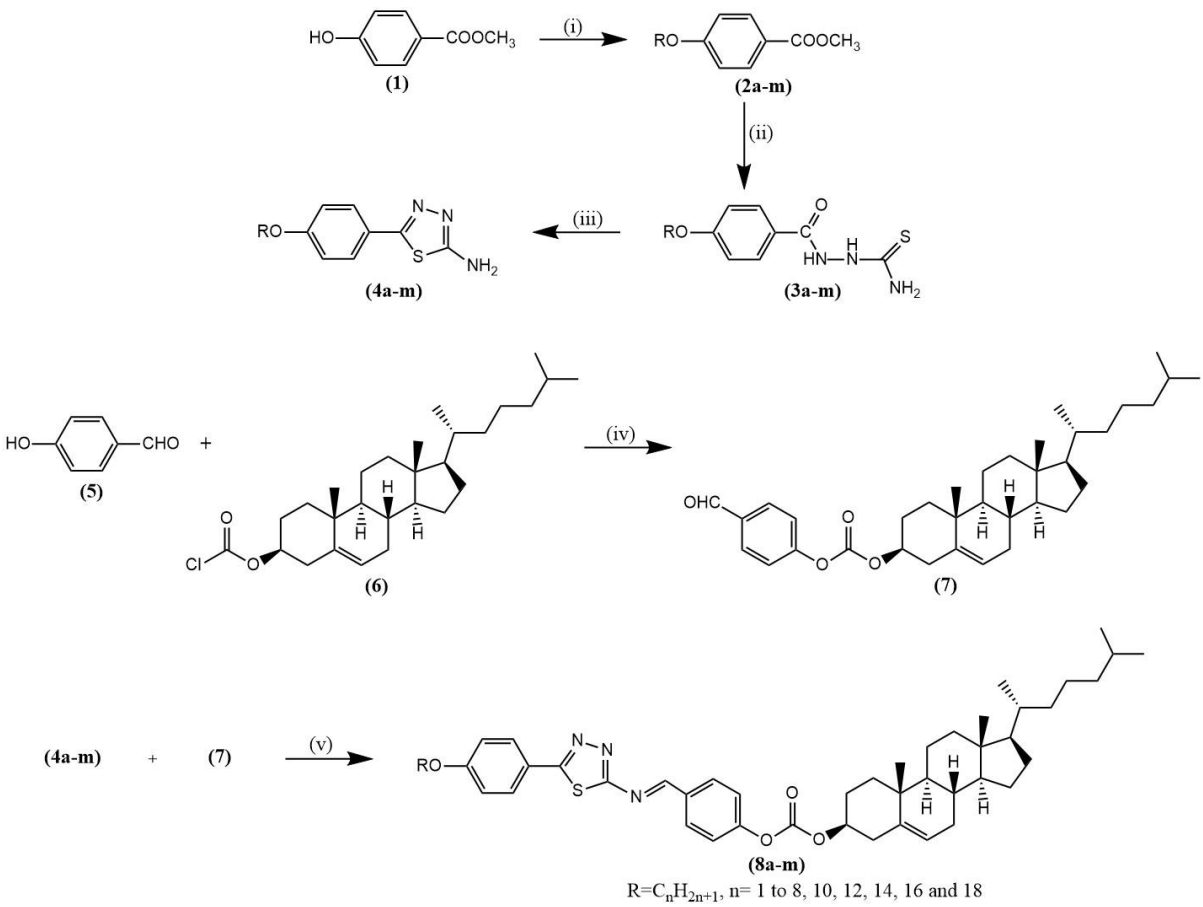

Scheme 4.1: Synthetic route for final Schiff's base derivatives (8a-m). Reagents and conditions; (i) DMF, K_2CO_3, appropriate R-Br, KI, reflux, 10-12 h; (ii) thiosemicarbazide, MeOH, reflux, 8-10 h; (iii) conc. H_2SO_4, 60-70°C, 6-8 h; (iv) dry THF, anhydrous pyridine, stirring at 38-40°C, 3-4 h; (v) chloroform: methanol (1:1), glacial acetic acid, 3-4 h.

*4.2.3.1. Synthesis of methyl 4-n-alkoxy benzoate **(2 a-m)***

The methyl 4-n-alkoxy benzoates **(2a-m)** were synthesised using the reported methods [45]. These esters were utilised to make the intermediate benzoyl thiosemicarbazides.

*4.2.3.2. Synthesis of 4-n-alkoxy benzoyl thiosemicarbazide **(3 a-m)***

The 4-n-alkoxy benzoyl thiosemicarbazides were synthesised according to reported procedure [46]. The thiosemicarbazide (0.015 mol) and methyl 4-n-alkoxy benzoates (0.01 mol) **(2a-m)** were dissolved in hot methanol (50 ml). Then, reaction mixture was refluxed for 8-10 h with an attached guard tube. The ice-water mixture was added to resulting solution. The solid separated was dried and recrystallized using ethanol.

*4.2.3.3. Synthesis 5-(4'-n-alkoxyphenyl)-2-amino-1,3,4-thiadiazole **(4 a-m)***

The 5-(4'-n-alkoxyphenyl)-2-amino-1,3,4-thiadiazoles were synthesised using the method described in literature [46–48]. In general, respective 4-n-alkoxy benzoyl thiosemicarbazides (0.01 mol) **(3a-m)** was added portion wise to concentrated sulphuric acid (20 ml) with continuous stirring. The mixture was heated at 60-70°C for 5 h and kept aside at room temperature overnight. The resulting solution was poured into ice- water mixture and made alkaline to pH 8 with liquor ammonia. The precipitated product was separated by filtration, washed thoroughly with distilled water and purified by recrystallization using ethanol to afford the desired product. Melting points are consistent with the reported value [29,49].

*4.2.3.4. Synthesis of 4-formyl phenyl cholesteryl carbonate **(7)**[40]*

Cholesteryl chloroformate (0.01 mol) **(6)** and dry THF (50 ml) were combined in a quick-fit round-bottom flask. To this mixture, 4-hydroxy benzaldehyde (0.011 mol) **(5)** was added, along with dry THF (40 ml) and anhydrous pyridine (4.0 ml) as a proton scavenger. The resulting mixture was stirred at around 38-40°C for 3-4 h with an attached guard tube. Afterward, the mixture was filtered to separate pyridinium chloride and other insoluble materials. The filtrate was then concentrated under vacuum to remove excess THF. Next, n-hexane was added to the solution for reprecipitation, and the mixture was filtered again. The precipitate product was subsequently recrystallized from an ethyl acetate-methanol mixture (60:40) until a consistent transition temperature was obtained.

Compound 7: White crystalline solid, yield 65%, phase transition temperatures: Cr 139.0°C N* 188.9°C Iso171.8°C N* 116°C Cr, IR (KBr, ν_{max}, cm^{-1}): 2943, 2888, 2868, 2851,

2790, 2720, 1755, 1703, 1502, 839; ^{1}H-NMR ($CDCl_3$, 400 MHz): δ (ppm) = 9.91 (s, 1H, CHO), 7.92-7.94 (d, 2H, J = 8.8 Hz, Ar-H), 7.30-7.32 (d, 2H, J = 8.8 Hz, Ar-H), 5.44-5.46 (m, 1H, -C=CH-), 4.58-4.66 (m, 1H, -OCH-CH_2), 2.52 (q, 2H, -OCH-CH_2), 0.70-2.05 (m for 41H, -CH, -CH_2 and -CH_3); ^{13}C NMR ($CDCl_3$, 400MHz): δ(ppm) = 191.2 (CHO), 158.36, 150.1 (-O-COO-), 158.36, 139.08, 134.19, 129.75, 122.22, 121.44, 79.13, 56.69, 56.13, 49.98, 42.33, 39.71, 39.53, 37.94, 36.84, 36.57, 36.19, 35.81, 31.92, 31.84, 28.24, 28.04, 27.65, 24.30, 23.84, 22.85, 22.58, 21.06, 19.31, 18.73, 11.84. Elemental analysis: calculated for $C_{35}H_{50}O_4$(%): C, 78.61; H, 9.42; found: C, 78.58, H; 9.46.

4.2.3.5. Synthesis of 5-(4'-n-alkoxy phenyl)-2-(4''-cholesteryl carbonate) benzylidene amino-1,3,4-thiadiazoles ***(8 a-m)***

A mixture of respective amino thiadiazole derivatives **(4a-m) (**0.002 mol) and 4-formyl phenyl cholesteryl carbonate **(7) (**0.002 mol) was refluxed in a mixture of $CHCl_3$/MeOH (v: v = 1:1) with a total volume of 20 ml for 8 h with an attached guard tube. To facilitate the reaction, glacial acetic acid (2-3 drops) was added as a catalyst. The progress of the reaction was monitored using TLC, which showed the disappearance of the starting materials. After refluxing, the reaction mixture was left to stand overnight, resulting in pale yellow crystals. These crystals were then filtered and recrystallized from a mixture of chloroform-methanol (40:60) until a constant transition temperature was achieved. The final product obtained was pale yellow in colour. The structure / purity data for one representative compound **8a** is shown below.

Compound 8a: Pale yellow crystalline solid, yield: 74.4%, IR (KBr, ν_{max}, cm^{-1}): 3033, 2946, 2898, 2866, 2844, 1754, 1624, 1506, 837; ^{1}H-NMR ($CDCl_3$, 400 MHz): δ(ppm) = 9.00 (s, 1H, CH=N), 7.93-7.95 (d, 2H, J = 8.8 Hz, Ar-H), 7.29-7.32 (d, 2H, J = 8.8 Hz, Ar-H), 7.23-7.25 (d, 2H, J = 8.8 Hz, Ar-H), 6.94-6.96 (d, 2H, J = 8.8 Hz, Ar-H), 5.44-5.48 (m, 1H, -C=CH-), 4.56-4.64 (m, 1H, -OC<u>H</u>-CH_2), 3.87 (s, 3H, -OCH_3), 2.50-2.54 (q, 2H, -OCH-C<u>H</u>$_2$), 0.70-2.05 (m for 41H, -CH, -CH_2 and -CH_3); ^{13}C NMR ($CDCl_3$, 400MHz): δ(ppm) = 173.4, 157.33 (CH=N), 156.03, 152.01, 151.58 (-O-COO-), 144.67, 139.11, 134.14, 129.69, 123.33, 122.26, 121.42, 114.38, 79.14, 55.68, 55.52, 55.16, 49.95, 42.36, 39.73, 39.51, 37.93, 36.85, 36.56, 36.21, 35.80, 31.92, 31.84, 28.24, 28.01, 27.56, 24.33, 23.84, 22.87, 22.58, 21.03, 19.34, 18.71, 11.86; Elemental analysis: calculated for $C_{44}H_{57}N_3O_4S$(%): C, 72.99; H, 7.94; N, 5.80; found: C, 73.12; H, 7.80; N, 5.96.

Compound 8b: Pale yellow crystalline solid, yield: 77.2%, IR (KBr, ν_{max}, cm^{-1}): 3044, 2944, 2906, 2866, 1756, 1626, 1509, 838; ^{1}H-NMR ($CDCl_3$, 400 MHz): δ(ppm) = 8.98 (s, 1H, CH=N), 7.92-7.94 (d, 2H, J = 8.4 Hz, Ar-H), 7.29-7.32 (d, 2H, J = 8.8 Hz, Ar-H), 7.24-7.26 (d, 2H, J = 8.8 Hz, Ar-H), 6.94-6.96 (d, 2H, J = 8.8 Hz, Ar-H), 5.42-5.46 (m, 1H, -C=CH-), 4.56-4.64 (m, 1H, -OC<u>H</u>-CH_2), 4.06-4.12(q, 2H, -CH_2-O-Ar), 2.50-2.52 (q, 2H, -OCH-C<u>H_2</u>), 0.70-2.05 (m, 44H, -CH, -CH_2 and -CH_3); ^{13}C NMR ($CDCl_3$, 400MHz): δ(ppm) = 173.6, 158.3 (CH=N), 153.4, 151.55 (-O-COO-), 143.5, 139.0, 134.15, 129.71, 123.32, 122.21, 121.6, 115.7, 79.12, 64.6, 55.71, 55.14, 49.95, 42.38, 39.71, 39.51, 37.93, 36.86, 36.57, 36.24, 35.81, 31.92, 31.85, 28.24, 28.02, 27.65, 24.27, 23.85, 22.86, 22.56, 21.07, 19.32, 18.72,13.81, 11.88; Elemental analysis: calculated for $C_{45}H_{59}N_3O_4S$(%): C, 73.23; H, 8.06; N, 5.69; found: C, 73.47; H, 8.28; N, 5.44.

Compound 8c: Pale yellow crystalline solid, yield: 81.8%, IR (KBr, ν_{max}, cm^{-1}): 3044, 2948, 2868, 1757, 1626, 1508, 842; ^{1}H-NMR ($CDCl_3$, 400 MHz): δ(ppm) = 8.97 (s, 1H, CH=N), 7.92-7.94 (d, 2H, J = 8.8 Hz, Ar-H), 7.30-7.32 (d, 2H, J = 8.8 Hz, Ar-H), 7.23-7.25 (d, 2H, J = 8.8 Hz, Ar-H), 6.93-6.95 (d, 2H, J = 8.8 Hz, Ar-H), 5.43-5.46 (m, 1H, -C=CH-), 4.58-4.66 (m, 1H, -OC<u>H</u>-CH_2), 3.98-4.01 (t, 2H, -CH_2-O-Ar), 2.50-2.52 (q, 2H, -OCH-C<u>H_2</u>), 0.70-2.05 (m, 46H, -CH, -CH_2 and -CH_3); ^{13}C NMR ($CDCl_3$,400MHz): δ(ppm) =172.98, 157.44 (CH=N), 156.73, 153.14, 151.61 (-O-COO-), 144.47, 139.04, 134.27, 129.78, 123.33, 122.12, 121.45, 115.0, 79.11, 68.27, 55.68, 55.13, 49.96, 42.32, 39.73, 39.52, 37.92, 36.84, 36.67, 36.29, 34.18, 31.39, 31.88, 29.00, 28.28, 28.01, 27.57, 24.39, 23.88, 22.84, 22.48, 22.51, 21.06, 19.33, 18.70, 14.15, 11.88; Elemental analysis: calculated for $C_{46}H_{61}N_3O_4S$(%): C, 73.46; H, 8.18; N, 5.59; found: C, 73.69; H, 8.01; N, 5.76.

Compound 8d: Pale yellow crystalline solid, yield: 78.4%, IR (KBr, ν_{max}, cm^{-1}): 3042, 2949, 2863, 1764, 1626, 1506, 841; ^{1}H-NMR ($CDCl_3$, 400 MHz): δ(ppm) = 8.99 (s, 1H, CH=N), 7.92-7.94 (d, 2H, J = 8.8 Hz, Ar-H), 7.30-7.32 (d, 2H, J = 8.8 Hz, Ar-H), 7.24-7.26 (d, 2H, J = 8.8 Hz, Ar-H), 6.93-6.95 (d, 2H, J = 8.8 Hz, Ar-H), 5.44-5.45 (m, 1H, -C=CH-), 4.58-4.66 (m, 1H, -OC<u>H</u>-CH_2), 3.94-3.98 (t, 2H, -CH_2-O-Ar), 2.50-2.52 (q, 2H, -OCH-C<u>H_2</u>), 0.70-2.05 (m, 48H, -CH, -CH_2 and -CH_3); ^{13}C NMR ($CDCl_3$, 400MHz): δ(ppm) =173.4, 157.39 (CH=N), 156.9, 152.08, 151.54 (-O-COO-), 144.6, 138.06, 133.19, 128.7, 123.38, 122.18, 121.7, 114.7, 79.18, 68.3, 55.78, 55.14, 47.94, 40.14, 38.77, 38.53, 37.00, 36.8, 36.52, 36.35, 34.89, 30.91, 30.84, 28.42, 28.13, 26.65, 24.19, 23.74, 22.86, 22.58, 20.07, 19.33, 17.73, 11.88,10.6; Elemental analysis: calculated for $C_{47}H_{63}N_3O_4S$(%): C, 73.69; H, 8.29; N, 5.49; found: C, 73.48; H, 8.55; N, 5.71.

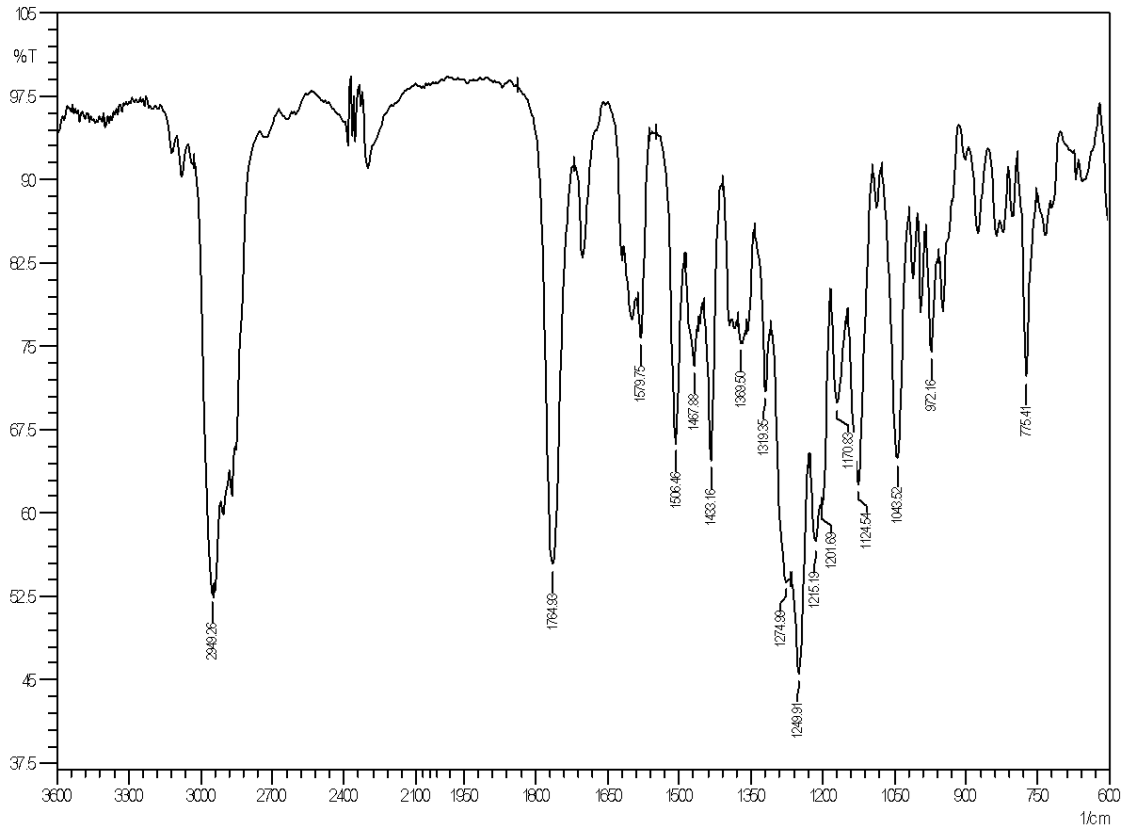

Figure 4.2 (a): IR Spectra of compound **8d**

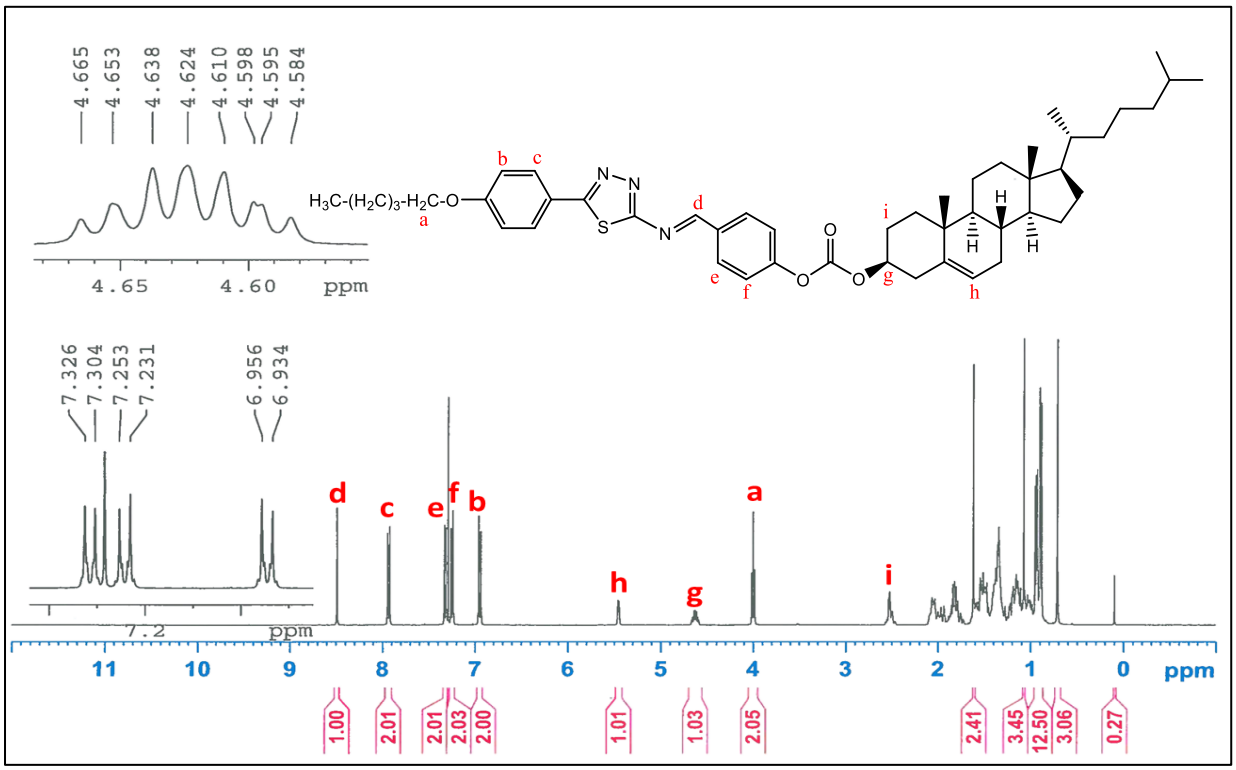

Figure 4.2 (b): ^{1}H-NMR Spectra of compound **8d**

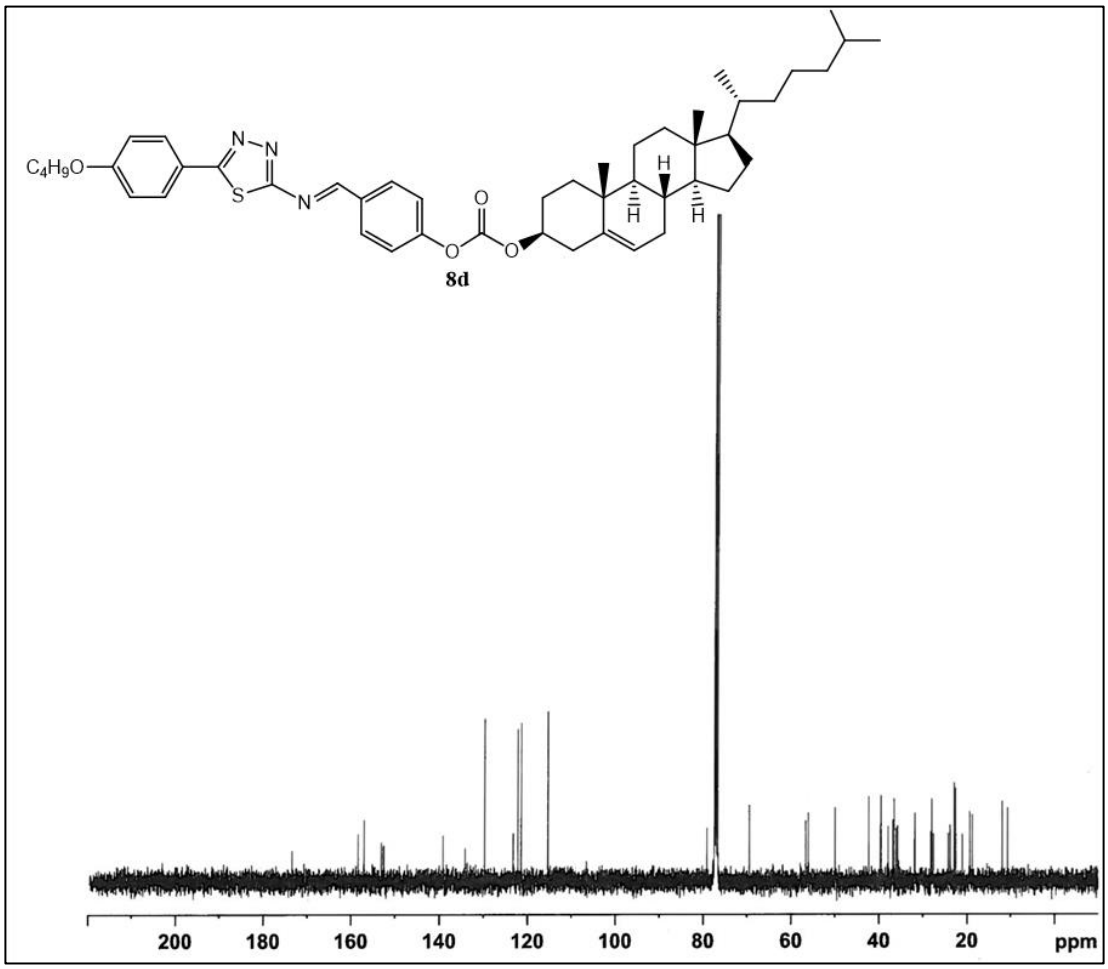

Figure 4.2 (c): ^{13}C-NMR Spectra of compound **8d**

Compound 8e: Pale yellow crystalline solid, yield: 76.8%, IR (KBr, ν_{max}, cm^{-1}): 3034, 2946, 2907, 2866, 1759, 1625, 1506, 838; ^{1}H-NMR ($CDCl_3$, 400 MHz): δ(ppm) = 8.99 (s, 1H, CH=N), 7.92-7.94 (d, 2H, J = 8.4 Hz, Ar-H), 7.30-7.32 (d, 2H, J = 8.4Hz, Ar-H), 7.23-7.25 (d, 2H, J = 8.8 Hz, Ar-H), 6.93-6.95 (d, 2H, J = 9.2 Hz, Ar-H), 5.44-5.45 (m, 1H, -C=CH-), 4.58-4.66 (m, 1H, -OC<u>H</u>-CH_2), 3.98-4.02 (t, 2H, -CH_2-O-Ar), 2.50-2.52 (q, 2H, -OCH-C<u>H</u>$_2$), 0.70-2.05 (m, 50H, -CH, -CH_2 and -CH_3); ^{13}C NMR ($CDCl_3$,400MHz): δ(ppm) =173.2, 156.8 (CH=N), 155.82, 152.07, 151.57 (-O-COO-), 144.47, 138.08, 133.24, 128.72, 123.38, 122.16, 121.44, 114.99, 79.12, 68.4, 55.69, 55.13, 49.78, 41.33, 39.78, 39.50, 37.93, 36.82, 36.52, 36.11, 35.88, 30.93, 30.85, 28.44, 28.14, 27.68, 24.30, 23.84, 22.88, 22.56, 22.48, 21.05, 19.32, 18.94, 14.13, 11.87; Elemental analysis: calculated for $C_{48}H_{65}N_3O_4S$(%): C, 73.90; H, 8.40; N, 5.39; found: C, 73.77; H, 8.29; N, 5.28.

Compound 8f: Pale yellow crystalline solid, yield: 82.6%, IR (KBr, ν_{max}, cm^{-1}): 3031, 2934, 2862, 1759, 1628, 1507, 838; ^{1}H-NMR ($CDCl_3$, 400 MHz): δ(ppm) = 8.98 (s, 1H, CH=N), 7.91-7.94 (d, 2H, J = 8.4 Hz, Ar-H), 7.30-7.32 (d, 2H, J = 8.8Hz, Ar-H), 7.23-7.25 (d, 2H, J = 8.8 Hz, Ar-H), 6.93-6.95 (d, 2H, J = 8.8 Hz, Ar-H), 5.44-5.45 (m, 1H, -C=CH-), 4.58-

4.66 (m, 1H, -OCH-CH_2), 3.97-4.01 (t, 2H, -CH_2-O-Ar), 2.50-2.52 (q, 2H, -OCH-CH_2), 0.70-2.05 (m, 52H, -CH, -CH_2 and -CH_3); ^{13}C NMR ($CDCl_3$,400MHz): δ(ppm) = 173.4, 157.98 (CH=N), 155.82, 152.04, 151.56 (-O-COO-), 144.46, 139.19, 133.25, 128.62, 123.32, 122.17, 121.46, 114.96, 79.13, 68.31, 55.69, 55.13, 49.98, 42.31, 39.75, 39.43, 37.95, 36.82, 36.55, 36.17, 35.83, 31.94, 31.87, 29.62, 29.58, 29.34, 29.31, 28.44, 28.14, 27.65, 26.07, 24.32, 23.83, 22.86, 22.70, 22.50, 21.07, 19.30, 18.96, 14.14, 11.87; Elemental analysis: calculated for $C_{49}H_{67}N_3O_4S$(%): C, 74.11; H, 8.50; N, 5.29; found: C, 73.97; H, 8.36; N, 5.52.

Compound 8g: Pale yellow crystalline solid, yield: 69.8%, IR (KBr, ν_{max}, cm^{-1}): 3035, 2935, 2868, 1757, 1626, 1508, 842; ^{1}H-NMR ($CDCl_3$, 400 MHz): δ(ppm) = 9.00 (s, 1H, CH=N), 7.92-7.94 (d, 2H, J = 8.4 Hz, Ar-H), 7.30-7.32 (d, 2H, J = 8.8 Hz, Ar-H), 7.23-7.25 (d, 2H, J = 8.8 Hz, Ar-H), 6.93-6.95 (d, 2H, J = 8.8 Hz, Ar-H), 5.44-5.45 (m, 1H, -C=CH-), 4.56-4.64 (m, 1H, -OCH-CH_2), 3.98-4.00 (t, 2H, -CH_2-O-Ar), 2.49-2.51 (q, 2H, -OCH-CH_2), 0.70-2.05 (m, 54H, -CH, -CH_2 and -CH_3); ^{13}C NMR ($CDCl_3$,400MHz): δ(ppm) = 173.8, 157.90 (CH=N), 156.84, 152.04, 151.58 (-O-COO-), 143.47, 139.18, 133.44, 129.75, 123.32, 122.24, 121.41, 114.99, 79.14, 68.19, 55.68, 55.13, 49.99, 41.34, 39.75, 39.49, 37.92, 36.80, 36.55, 36.17, 35.80, 31.95, 31.87, 29.40, 29.11, 28.38, 28.14, 27.67, 24.32, 23.88, 22.82, 22.56,22.30, 21.07, 19.29, 18.68, 14.14, 11.88; Elemental analysis: calculated for $C_{50}H_{69}N_3O_4S$(%): C, 74.31; H, 8.61; N, 5.20; found: C, 74.08; H, 8.48; N, 5.44.

Compound 8h: Pale yellow crystalline solid, yield: 66.0%, IR (KBr, ν_{max}, cm^{-1}): 3042, 2951, 2924, 2888, 2852, 1759, 1624, 1508, 842; ^{1}H-NMR ($CDCl_3$, 400 MHz): δ(ppm) = 9.00 (s, 1H, CH=N), 7.92-7.94 (d, 2H, J = 8.4 Hz, Ar-H), 7.30-7.32 (d, 2H, J = 8.8 Hz, Ar-H), 7.23-7.25 (d, 2H, J = 8.8Hz, Ar-H), 6.93-6.95 (d, 2H, J = 8.8 Hz, Ar-H), 5.44-5.45 (m, 1H, -C=CH-), 4.58-4.66 (m, 1H, -OCH-CH_2), 3.97-4.01 (t, 2H, -CH_2-O-Ar), 2.50-2.52 (q, 2H, -OCH-CH_2), 0.70-2.05 (m, 56H, -CH, -CH_2 and -CH_3); ^{13}C NMR ($CDCl_3$,400MHz): δ(ppm) = 173.98, 156.99(CH=N), 155.81, 152.04, 151.57 (-O-COO-), 144.50, 139.11, 134.19, 129.68, 123.29, 122.21, 121.44, 114.99, 79.12, 68.29, 55.68, 55.12, 49.99, 42.31, 39.69, 39.51, 37.90, 36.81, 36.57, 36.20, 35.79, 31.88, 31.81, 31.79, 29.32, 29.09, 28.31, 28.14, 27.66, 24.30, 23.82, 22.87, 22.68, 22.54, 22.39, 21.17, 19.38, 18.72, 14.14, 11.87; Elemental analysis: calculated for $C_{51}H_{71}N_3O_4S$(%): C, 74.50; H, 8.70; N, 5.11; found: C, 74.37; H, 8.62; N, 5.30.

Compound 8i: Pale yellow crystalline solid, yield: 75.7%, IR (KBr, ν_{max}, cm^{-1}): 3033, 2936, 2850, 1757, 1624, 1505, 838; ^{1}H-NMR ($CDCl_3$, 400 MHz): δ(ppm) = 9.00 (s, 1H, CH=N), 7.92-7.94 (d, 2H, J = 8.4 Hz, Ar-H), 7.30-7.32 (d, 2H, J = 8.8 Hz, Ar-H), 7.23-7.25 (d, 2H, J = 9.2 Hz, Ar-H), 6.93-6.95 (d, 2H, J = 9.2 Hz, Ar-H), 5.44-5.45 (m, 1H, -C=CH-),

4.59-4.64 (m, 1H, -OCH-CH_2), 3.97-3.99 (t, 2H, -CH_2-O-Ar), 2.50-2.52 (q, 2H, -OCH-CH_2), 0.70-2.05 (m, 60H, -CH, -CH_2 and -CH_3); ^{13}C NMR ($CDCl_3$,400MHz): δ(ppm) = 174.00, 157.99 (CH=N), 156.81, 152.04, 151.57 (-O-COO-), 144.39, 139.11, 135.24, 129.68, 123.27, 122.21, 121.13, 114.99, 79.14, 68.32, 55.69, 55.13, 49.97, 42.43, 39.81, 39.62, 37.84, 36.92, 36.55, 36.21, 35.79, 31.88, 31.75, 31.61, 29.32, 29.08, 28.28, 28.01, 27.65, 24.29, 23.81, 22.95, 22.83, 22.51, 21.07, 19.20, 18.88, 14.13, 11.88; Elemental analysis: calculated for $C_{53}H_{75}N_3O_4S$(%): C, 74.87; H, 8.89; N, 4.94; found: C, 74.71; H, 8.67; N, 5.09.

Compound 8j: Pale yellow crystalline solid, yield: 78.0%, IR (KBr, ν_{max}, cm^{-1}): 3028, 2924, 2859, 1755, 1624, 1504, 834; ^{1}H-NMR ($CDCl_3$, 400 MHz): δ(ppm) = 9.00 (s, 1H, CH=N), 7.91-7.94 (d, 2H, J = 8.8 Hz, Ar-H), 7.30-7.32 (d, 2H, J = 8.8 Hz, Ar-H), 7.23-7.25 (d, 2H, J = 8.8 Hz, Ar-H), 6.93-6.95 (d, 2H, J = 8.8 Hz, Ar-H), 5.44-5.45 (m, 1H, -C=CH-), 4.58-4.66 (m, 1H, -OCH-CH_2), 3.97-4.01 (t, 2H, -CH_2-O-Ar), 2.49-2.52 (q, 2H, -OCH-CH_2), 0.70-2.05 (m, 64H, -CH, -CH_2 and -CH_3); ^{13}C NMR ($CDCl_3$,400MHz): δ(ppm) = 173.98, 156.99 (CH=N), 155.81, 152.04, 151.57 (-O-COO-), 144.54, 139.18, 133.18, 129.68, 123.37, 122.21, 121.38, 114.99, 79.11, 68.31, 55.69, 55.13, 49.99, 42.33, 39.70, 39.43, 37.84, 36.96, 36.65, 36.21, 34.81, 31.91, 31.78, 29.61, 29.58, 29.48, 29.43, 29.11, 29.34, 29.29, 29.22, 28.35, 28.12, 27.66, 25.07, 24.42, 23.72, 22.65, 22.51, 22.45, 21.00, 19.29, 18.96, 14.14, 11.87; Elemental analysis: calculated for $C_{55}H_{79}N_3O_4S$(%): C, 75.21; H, 9.07; N, 4.78; found: C, 74.99; H, 8.92; N, 4.55.

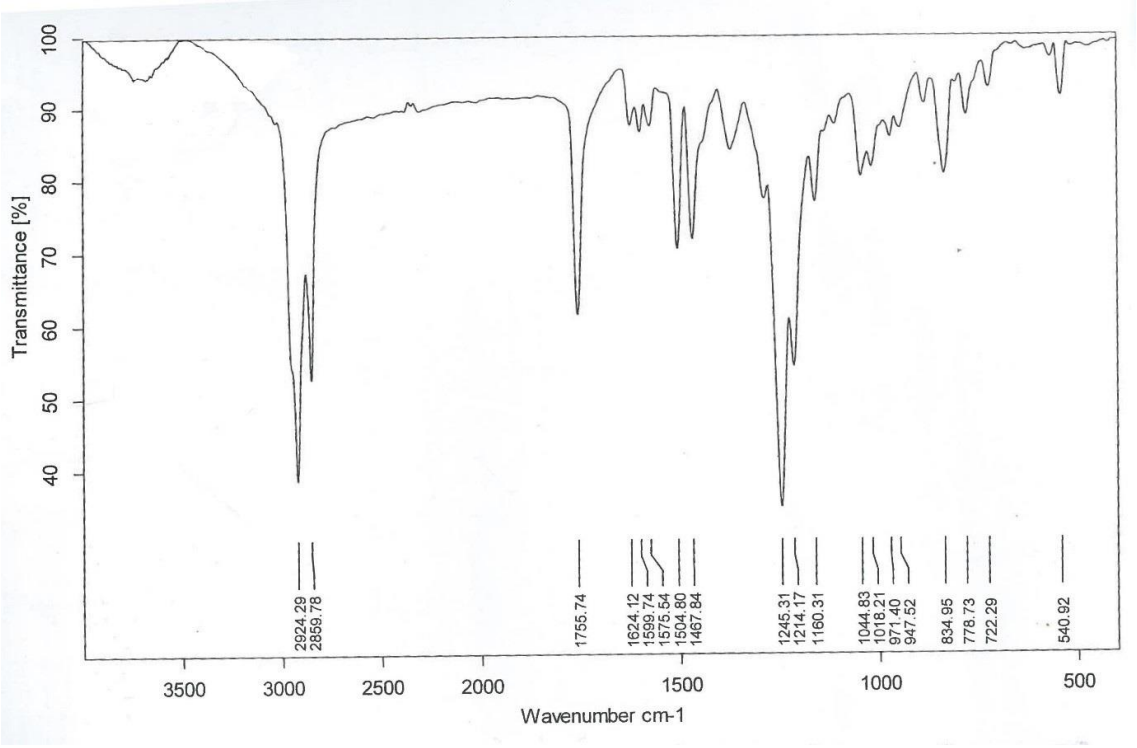

Figure 4.3 (a): IR Spectra of compound **8j**

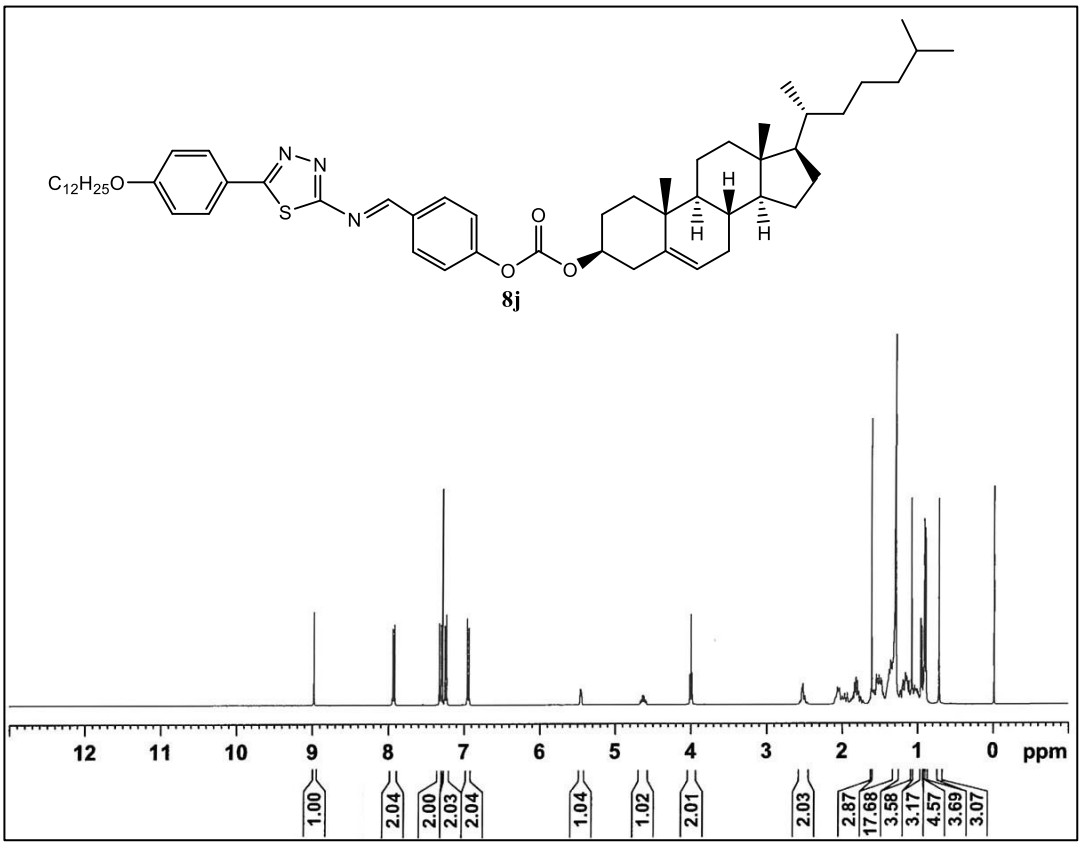

Figure 4.3 (b): ^{1}H-NMR Spectra of compound **8j**

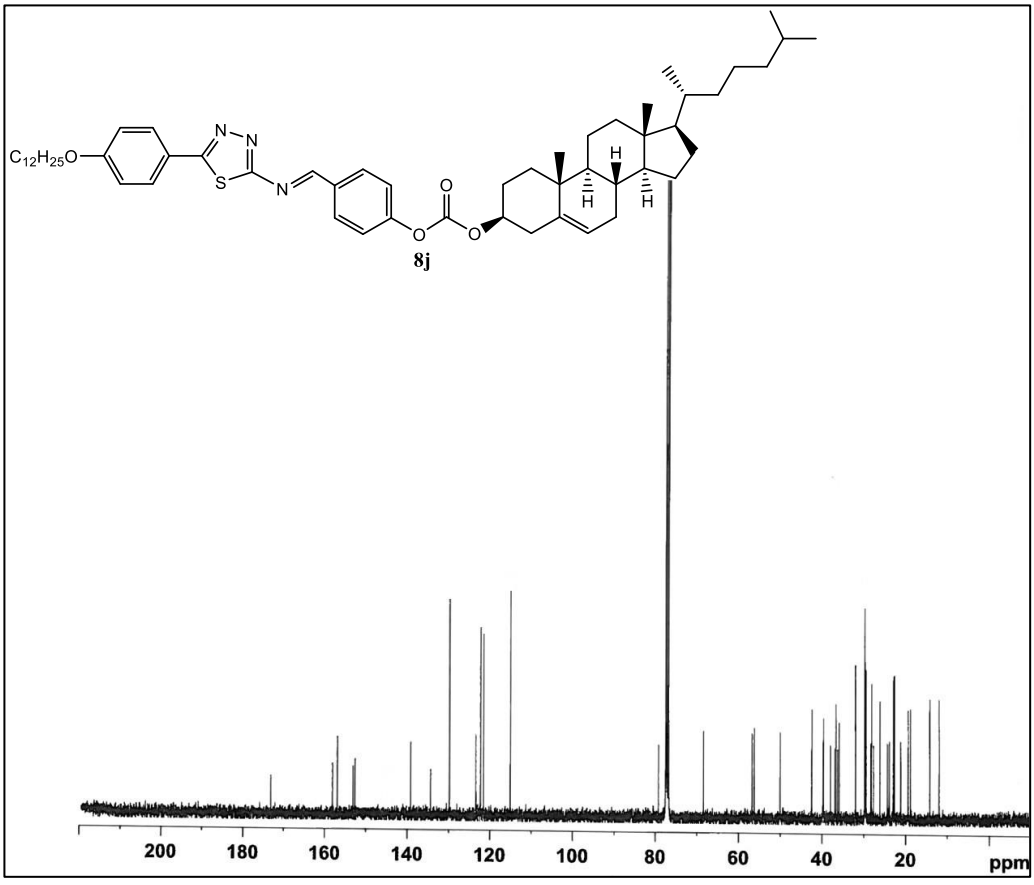

Figure 4.3 (c): ^{13}C-NMR Spectra of compound **8j**

Compound 8k: Pale yellow crystalline solid, yield: 80.2%, IR (KBr, ν_{max}, cm^{-1}): 3029, 2963, 2920, 2850, 1757, 1626, 1508, 831; ^{1}H-NMR ($CDCl_3$, 400 MHz): δ(ppm) = 8.99 (s, 1H, CH=N), 7.91-7.94 (d, 2H, J = 8.8 Hz, Ar-H), 7.30-7.32 (d, 2H, J = 8.4 Hz, Ar-H), 7.23-7.25 (d, 2H, J = 8.8 Hz, Ar-H), 6.93-6.95 (d, 2H, J = 8.8 Hz, Ar-H), 5.44-5.45 (m, 1H, -C=CH-), 4.58-4.66 (m, 1H, -OC<u>H</u>-CH_2), 3.97-4.00 (t, 2H, -CH_2-O-Ar), 2.49-2.52 (q, 2H, -OCH-C<u>H_2</u>), 0.70-2.05 (m, 68H, -CH, -CH_2 and -CH_3); ^{13}C NMR ($CDCl_3$,400MHz): δ(ppm) = 173.88, 156.97 (CH=N), 155.83, 152.04, 151.56 (-O-COO-), 144.46, 139.18, 133.34, 129.83, 123.41, 122.23, 121.40, 114.99, 79.14, 68.42, 55.73, 55.23, 49.97, 41.46, 39.81, 39.42, 37.98, 36.82, 36.45, 36.07, 34.78, 31.90, 31.83, 29.70, 29.49, 29.35, 29.26, 29.21, 28.16, 28.01, 27.66, 26.28, 24.50, 23.92, 22.84, 22.68, 22.41, 21.16, 19.30, 18.96, 14.1, 11.87; Elemental analysis: calculated for $C_{57}H_{83}N_3O_4S$(%): C, 75.54; H, 9.23; N, 4.64; found: C, 75.38; H, 9.07; N, 4.42.

Compound 8l: Pale yellow crystalline solid, yield: 82.4%, IR (KBr, ν_{max}, cm^{-1}): 3036, 2926, 2853, 1757, 1624, 1505, 884; ^{1}H-NMR ($CDCl_3$, 400 MHz): δ(ppm) = 9.00 (s, 1H, CH=N), 7.91-7.94 (d, 2H, J = 8.8 Hz, Ar-H), 7.30-7.32 (d, 2H, J = 8.8 Hz, Ar-H), 7.23-7.25 (d, 2H, J = 8.8 Hz, Ar-H), 6.93-6.95 (d, 2H, J = 8.8 Hz, Ar-H), 5.44-5.45 (m, 1H, -C=CH-), 4.61-4.64 (m, 1H, -OC<u>H</u>-CH_2), 3.97-4.00 (t, 2H, -CH_2-O-Ar), 2.50-2.52 (q, 2H, -OCH-C<u>H_2</u>), 0.70-2.05 (m, 72H, -CH, -CH_2 and -CH_3); ^{13}C NMR ($CDCl_3$,400MHz): δ(ppm) = 173.98, 156.98 (CH=N), 155.81, 152.04, 151.57 (-O-COO-), 144.52, 139.29, 135.14, 129.81, 123.29, 122.23, 121.48, 114.99, 79.33, 68.34, 55.59, 55.43, 49.97, 41.42, 39.81, 39.60, 37.91, 36.82, 36.77, 36.29, 34.71, 31.99, 31.77, 31.22, 29.83, 29.79, 29.65, 29.60, 29.59, 29.55, 29.40, 29.31, 29.28, 28.20, 28.01, 27.65, 26.17, 24.28, 23.82, 22.95, 22.80, 22.66, 21.16, 19.29, 18.96, 14.13, 11.87. Elemental analysis: calculated for $C_{59}H_{87}N_3O_4S$(%): C, 75.84; H, 9.39; N, 4.50; found: C, 75.59; H, 9.14; N, 4.38.

Compound 8m: Pale yellow crystalline solid, yield: 80.6%, IR (KBr, ν_{max}, cm^{-1}): 3034, 2958, 2849, 1761, 1626, 1508, 839; ^{1}H-NMR ($CDCl_3$, 400 MHz): δ(ppm) = 8.99 (s, 1H, CH=N), 7.91-7.94 (d, 2H, J = 8.8 Hz, Ar-H), 7.30-7.32 (d, 2H, J = 8.8 Hz, Ar-H), 7.23-7.25 (d, 2H, J = 8.8 Hz, Ar-H), 6.93-6.95 (d, 2H, J = 8.8 Hz, Ar-H), 5.44-5.45 (m, 1H, -C=CH-), 4.61-4.64 (m, 1H, -OC<u>H</u>-CH_2), 3.97-4.00 (t, 2H, -CH_2-O-Ar), 2.50-2.51 (q, 2H, -OCH-C<u>H_2</u>), 0.70-2.05 (m, 76H, -CH, -CH_2 and -CH_3); ^{13}C NMR ($CDCl_3$,400MHz): δ(ppm) = 173.99, 156.89 (CH=N), 155.87, 152.24, 151.43 (-O-COO-), 144.52, 139.01, 133.36, 129.63, 123.40, 122.21, 121.38, 114.98, 79.11, 68.34, 55.77, 55.05, 49.98, 41.49, 39.82, 39.48, 37.88, 36.79, 36.61, 36.21, 35.79, 31.88, 31.56, 29.83, 29.79, 29.66, 29.55, 29.53, 29.48, 29.44, 29.33, 29.29, 28.21, 28.02, 27.54, 26.16, 24.28, 23.79, 22.78, 22.63, 22.25, 21.06, 19.28, 18.96, 14.13, 11.87;

Elemental analysis: calculated for $C_{61}H_{91}N_3O_4S$(%): C, 76.12; H, 9.53; N, 4.37; found: C, 75.98; H, 9.40; N, 4.55.

4.3. Results and discussion

4.3.1. Structural characterisation

The final azomethine compounds **(8a-m)** were prepared using condensation reaction of 4-formyl phenyl cholesteryl carbonate **(7)** with the appropriate 5-(4'-n-alkoxyphenyl)-2-amino-1,3,4-thiadiazole **(4a-m)**. The synthetic route adopted is given in Scheme 1. All the compounds in the series show mesogenic behaviour. The methyl to n-butyl derivatives show oily streak texture of cholesteric (chiral nematic-N*) phase in heating as well as cooling rounds. The n-pentyl and n-hexyl derivatives also exhibited chiral nematic mesophase. Moreover, on gradually cooling from isotropic melt an additional SmA phase was observed. The n-heptyl to n-decyl homologues exhibited enantiotropic SmA-N*-Isotropic phase transition. The SmA-N* transition in n-pentyl to n-decyl derivatives were accompanied by an interceding frustrated mesophase (TGB_A-twist grain boundary). The higher derivatives from n-dodecyl to n-octadecyl show an enantiotropic SmC*-SmA-Isotropic transition. The DSC thermograms are in comparable agreement with the polarizing optical microscopy. Compounds were also thermally stable up to 341-378°C as analysed thermogravimetrically.

The FT-IR and NMR spectra, as well as the elemental analyses, are in complete agreement with the structure. In FT-IR spectra, compound 4-formyl phenyl cholesteryl carbonate **(7)** displayed prominent bands (ν_{max}, cm^{-1}) at 2943, 2888, 2868, 2851 (CH aliphatic), 2720 (CH stretch aldehyde),1755 (CO carbonate), 1703 (CO stretch aldehyde), 1450-1500 (Ph), 1575 cm^{-1} (C-C aromatic) stretch. The compound **(8a)** exhibits major IR bands at 2944, 2847 (CH aliphatic), 1753 (CO carbonate), and 1623 (CH=N azomethine) after condensation with 5-(4'-n-methoxyphenyl)-2-amino-1,3,4-thiadiazole **(4a)**. The disappearance of bands at 1703 and 2720 cm^{-1} due to aldehyde (CHO) and the appearance of a new band at 1623 cm^{-1} due to azomethine (CH=N) indicate condensation of aldehyde with amine to form Schiff base, validating the structure of the compound 5-(4'-n-methoxy phenyl)-2-(4"-cholesteryl carbonate) benzylidene amino-1,3,4-thiadiazole **(8a)**.

The proton NMR of compound **(7)** displayed a prominent signal at δ9.91 (s, 1H, -CHO) ppm of the aldehyde group. The proton NMR of the final Schiff's base 5-(4'-n-methoxy phenyl)-2-(4"-cholesteryl carbonate) benzylidene amino-1,3,4-thiadiazole **(8a)** depicts signals

at δ8.98 (s, 1H, -CH=N), δ7.94-6.94 (m, 8H, Ar-H), δ5.5 (m, 1H, olefinic H in cholesterol), δ4.6 (m, 1H, H of cholesterol near carbonate linkage), δ3.86 (s, 3H, -OCH_3), δ2.5 (d, 2H, -OCH-C$\underline{H}_2$), δ2.05-0.70 (m for 41H, -CH,-CH_2 and -CH_3 of cholesterol) ppm, respectively. The disappearance of the singlet at δ9.91 ppm and appearance of a characteristic signal due to the azomethine group at δ8.98 ppm confirm the formation of 5-(4'-n-methoxy phenyl)-2-(4''-cholesteryl carbonate) benzylidene amino-1,3,4-thiadiazole **(8a)**. The ^{13}C NMR spectrum of the compound **(7)** depicts prominent peaks at δ191.2 (CHO) and δ150.1(-O-COO-) ppm, whilst the compound **(8a)** exhibits signal at δ173.4 (C_5 thiadiazole), δ157.33 (azomethine carbon CH=N), δ151.58 (carbonate carbon -O-COO-), and δ129.75-114.40 (carbons of aromatic rings) ppm. Thus, the appearance of azomethine carbon (CH=N) **(8a)** at δ157.33 ppm confirms the formation of Schiff base **(8a)**.

The rest of the members in the series displayed similar IR and NMR (^1H and ^{13}C) spectra, which are outlined in the synthetic part.

4.3.2. Texture analysis

The optical textures of the Schiff's bases **8a-m** were examined by using POM equipped with heating stage, for observing the characteristic textures for identification of mesomorphic phases. Their representative textures were shown in **Figure 4.4**. All compounds show liquid crystalline behaviour and were stable during the process of repeated heating and cooling.

In the series of compounds, the lower homologues, **8a-d** when heated, it melted and displayed a characteristic typical oily streaks texture of cholesteric [50] (chiral nematic mesophase-N*) phase as seen in **Figure 4.4 (a)**. This texture persisted until the compound transitioned to the isotropic phase. Upon cooling from the isotropic phase, the droplet-shaped nematic texture reappeared which gradually combined, and transformed into the nematic schlieren texture as depicted in **Figure 4.4 (b)**, which looks similar to that of SmA mesophase but on mechanical shearing changes into distinctive Grandjean planar texture [51] under the crossed polarizers. Because the pitch of the cholesteric phase is significantly dependent on the temperature, due to the selective reflection phenomenon, the reflection of different colours in the visible range is noticed in cholesteric mesophase as the temperature is lower [52]. This distinctive texture remained visible until the sample crystallized. This compound falls within the category of thermotropic enantiotropic chiral nematic liquid crystals. Compounds **8e** and **8f** in heating cycle exhibited an oily streaks texture of chiral nematic (N*) phase until isotropic, similar to the lower homologues, but in cooling cycle first a N* phase was observed which on

further cooling transformed into a dark field view of Smectic A (Sm-A) mesophase, which proceeds through frustrated phase known as twist grain boundary phase (TGB_A).

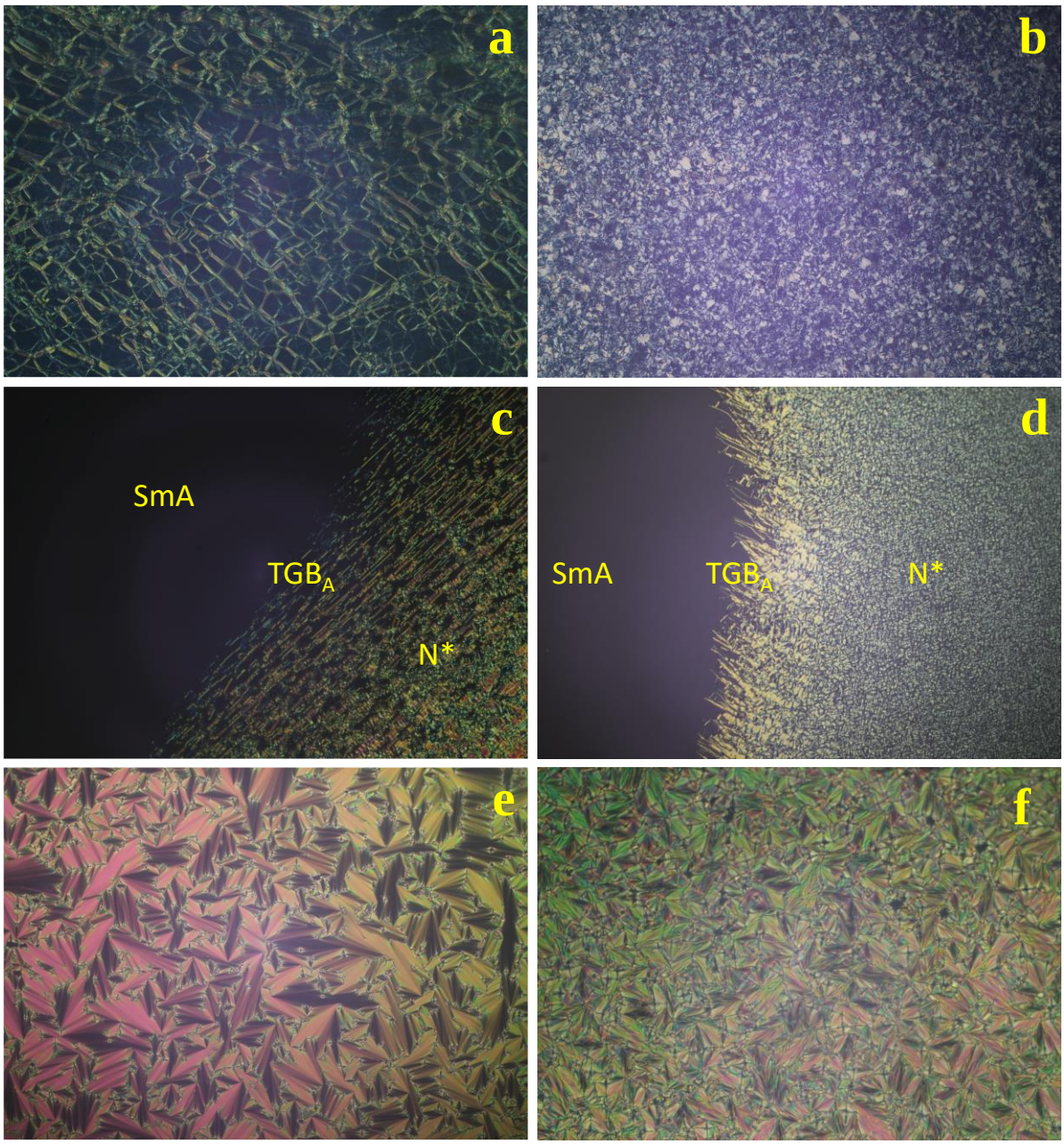

Figure 4.4: Microphotographs of the textures observed under POM for the different LC phases of compounds placed between two untreated glass substrates **(a)** Oily streaks texture of cholesteric or chiral nematic (N*) phase of **8a** at 171°C, **(b)** nematic (N*) schlieren texture of **8d** at 275°C, **(c)** filament texture of SmA-TGB_A-N* transition of **8g** at 250°C, **(d)** filament texture of SmA-TGB_A-N* transition of **8i** at 265°C, **(e)** fan shaped texture of SmA mesophase of **8k** at 270°C **(f)** broken fan shaped texture with helix lines of SmC* phase of **8l** at 156°C

The existence of the transient TGB_A phase is visually confirmed through optical observations. Under crossed polarizers, the growth of filament-like textures is noticeable, as depicted in **Figure 4.4 (c)**. This appearance closely resembles the textures documented in existing literature [53–55]. Compounds **8g-i** exhibited enantiotropic cholesteric (N*) and smectic A (SmA) mesophases, appearing as dark regions due to the alignment of the optic axis in the direction of light propagation [53], along with an intervening TGB_A phase. Under homeotropic boundary condition, the existence of transitory TGB_A phase may be clearly distinguished by the unique filamentary texture [38] between homeotropically aligned SmA mesophase (dark region) and the N* phase **(Figure 4.4 (d))**. The frustration in the above discussed mesogenic compounds arises from the inherent conflict between the desire for certain molecular orientations or arrangements and the restrictions imposed by the geometry and interactions of the molecules themselves and also external factors such as temperature, pressure or electric fields, which prevents the aligning of the molecules in the regular pattern, which results into the complex arrangement of molecular orientations, often leading to unique optical properties.

The higher homologues of the series **8j-m** on heating first shows a Smectic C* (SmC*) mesophase which on further heating transformed from tilted, helical structure of Smectic C* to the untwisted, parallel structure of Smectic A observed as fan shaped texture and maintained until isotropic. In the cooling cycle the compounds exhibited SmA phase **(Figure 4.4 (e))**, although not observed clearly in DSC thermogram on further cooling these compounds exhibited broken fan shaped texture with equidistant line pattern due to the helical superstructure resembling SmC* phase **(Figure 4.4 (f))** as observed through POM [56,57].

Table 4.1: Phase transition temperature of compounds **8a-m** [a, b]

Sample code	n-alkyl chain	Heating Temp °C [ΔH kJ mol^{-1}]	Cooling Temp °C [ΔH kJ mol^{-1}]
8a	**1**	Cr 157.7 [26.96] N* 304.3 [1.20] I	I 298.0 [1.28] N* 91.3 [22.89] Cr
8b	**2**	Cr 183.0 [27.01] N* 314.1 [1.28] I	I 305.7 [1.36] N* 85.5 [24.44] Cr
8c	**3**	Cr 216.0 [43.76] N* 299.8 [1.64] I	I 289.8 [1.62] N* 93.4 [34.37] Cr

8d	**4**	Cr 232.6 [35.44] N* 301.6 [1.06] I	I 295.2 [1.23] N* 106.3 [30.83] Cr
8e	**5**	Cr 244.8 [31.57] N* 294.7 [1.13] I	I 288.7 [0.97] N* (204.5) [1.08] TGB_A-SmA[c,d] 95.9 [29.38] Cr
8f	**6**	Cr 252.3 [34.11] N* 292.8 [1.19] I	I 284.0 [0.88] N* (225.1) [0.94] TGB_A-SmA[c,d] 99.7 [30.36] Cr
8g	**7**	Cr 231.3 [22.86] SmA- TGB_A[c,d] 256.4 [0.97] N* 288.7 [0.83] I	I 285.8 [0.75] N* 251.4 [1.18] TGB_A-SmA[c,d] 73.4 [16.31] Cr
8h	**8**	Cr 242.3 [37.30] SmA- TGB_A[c,d] 263.7 [1.18] N* 285.3 [1.23] I	I 279.4 [0.99] N* 247.6 [0.93] TGB_A-SmA[c,d] 76.0 [29.23] Cr
8i	**10**	Cr 248.7 [34.80] SmA- TGB_A[c,d] 270.1 [0.96] N* 282.1 [0.85] I	I 278.7 [1.02] N* 265.1 [0.98] TGB_A-SmA[c,d] 72.6 [27.39] Cr
8j	**12**	Cr 152.5 [37.06] SmC* 262.4 [0.53] SmA 277.0 [14.21] I	I 276.3 [12.38] SmA 119.8 [0.66] SmC* 75.4 [27.48] Cr
8k	**14**	Cr 144.5 [41.78] SmC* 258.6 [0.31] SmA 271.2 [11.93] I	I 268.7 [16.08] SmA 114.1 SmC*[d] 77.7 [23.10] Cr
8l	**16**	Cr 138.2 [36.00] SmC* 251.0 SmA[d] 265.1 [18.96] I	I 263.8 [13.98] SmA 110.0 SmC*[d] 68.3 [28.21] Cr
8m	**18**	Cr 128.4 [42.65] SmC* 239.5 SmA[d] 262.8 [21.38] I	I 259.3 [22.17] SmA 111.4 SmC*[d] 70.1 [34.91] Cr

Cr = crystal, Sm = smectic phase, N* = chiral nematic/ cholesteric phase, TGB_A = twist grain boundary A phase, I = isotropic.

[a]Phase transition temperatures were determined/confirmed by both polarizing optical microscope (POM) and differential scanning calorimetry (DSC) studies: peak temperatures in the DSC thermograms obtained during the first heating and cooling cycles (scanning rate = 5°C min-1) coupled with POM measured temperatures are given; [b]Transition temperatures of some of the compounds were determined with the aid of a POM study as the expected well-resolved thermograms of both heating and cooling cycles could not be obtained; [c]Although TGB_A–SmA/ SmA–TGB_A phase transitions were observed in POM, they were not resolved in DSC traces; hence the enthalpy value represents the combined enthalpy for TGB_A–SmA/ SmA–TGB_A transitions; [d]Phase transition was observed under POM; enthalpy change too weak to be detected by DSC.

4.3.3. Thermal properties

The phase transition temperatures, enthalpy changes, and mesophase textures of the individual compounds **8a-m** are concisely presented in **Table 4.1**. DSC analyses (**Figure 4.5.(a** and **b))** coupled with observations using POM provided clear transition temperatures and textures for the entire series of compounds, and they were in reasonable agreement with each other over the many heating/cooling cycles.

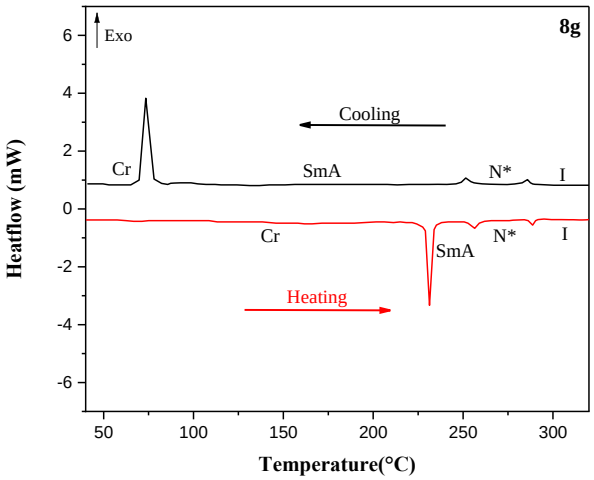

Figure 4.5 (a): DSC thermogram of **8g**

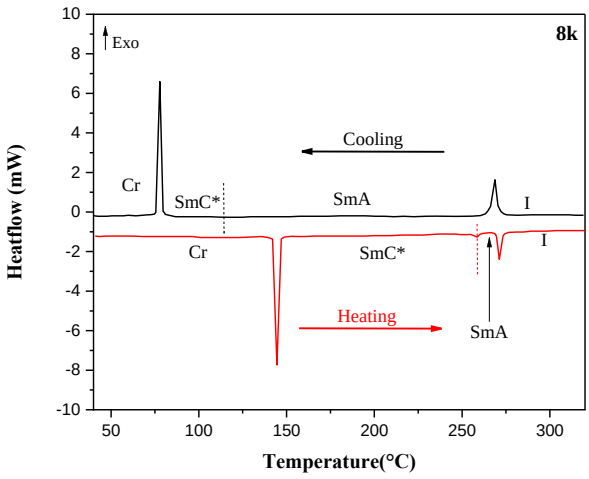

Figure 4.5 (b): DSC thermogram of **8h**

Compounds **8a-d** displayed two endothermic and two exothermic peaks in both heating and cooling cycles respectively, of which one showed a very low enthalpy change. This peak with the low enthalpy change can be assigned to the N*-Isotropic transition as it is a reflection of the relatively weak molecular interactions in the nematic phase, which require less energy to be disrupted as the system moves into the isotropic phase, and the peak with the higher enthalpy change can be assigned to the Cr-N* phase transition. Compound **8e** and **8f** shows two endotherms in heating cycle and three endotherms in cooling cycle. On heating the first transition was observed from Cr to N* mesophase and second for N* to Isotropic with relatively low ΔH value. In cooling cycle first and second transition with lower ΔH value corresponds to isotropic to N* transition and N* to SmA transition respectively. While third exothermic peak corresponds to SmA to Cr transition. Compounds **8g-i** shows three endothermic and three exothermic peaks corresponding to Cr-(SmA-TGB_A), (SmA-TGB_A) -N* and N*-Isotropic transition both in heating and cooling cycles. Although TGB_A–SmA/ SmA–TGB_A phase transitions were observed in POM, they were not resolved in DSC thermograms, because the transitions between these phases are due to competing intermolecular interactions and strong molecular chirality, as observed in the thermograms therefore ΔH value represents the combined enthalpy for TGB_A–SmA/ SmA–TGB_A transitions. Compounds **8j-m** displayed two

endothermic and two exothermic which corresponds to Cr-SmA and SmA-Isotropic transition in both heating and cooling cycles. An additional SmC* phase was observed for **8j-m** using polarizing optical microscopy. In some of the compounds **(8j and 8k)** a minor peak in thermograms was observed with negligible ΔH value, as the primary change occurs in the molecular arrangement and orientation within the layers rather than a disruption or forming of the bonds, which does not involve a substantial enthalpy change as observed in thermograms.

Enthalpy changes are fairly predictable during the initial transition from crystal to chiral nematic or smectic A phases for all the compounds outlined in **Table 4.1**. However, when it comes to the transition from chiral nematic to isotropic phases, the observed enthalpy changes are less significant than what was predicted. Again, this is to be expected with these kinds of mesogens [33,57]. Also, the large enthalpy values for the smectic A to isotropic transition compared to the chiral nematic to isotropic transition are possibly due to the higher degree of order in the smectic mesophase, which involves a more significant reorganisation of molecular packing, leading to a larger enthalpy for the phase transition. This is supported by the recorded enthalpy values for the transitions, where the SmA-Iso transition enthalpy values are significantly larger than the N-Iso transition enthalpy values [58–60].

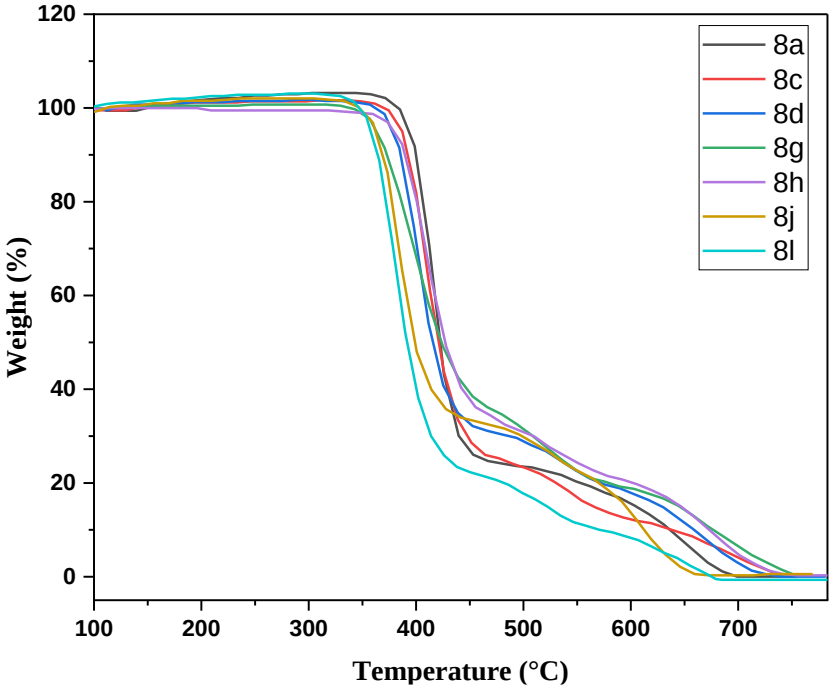

Figure 4.6: TGA profile for some of the cholesterol derivatives

Thermogravimetric analysis (TGA) was used to evaluate the thermal stability of compounds **8a**, **8c**, **8d**, **8g**, **8h**, **8j**, and **8l**. When exploring their mesomorphic properties, it was observed that all the cholesterol derivatives remained stable at temperatures ranging from 341 to 378°C. However, it's worth noting that these cholesterol derivatives did experience

decomposition when subjected to repeated heating and cooling cycles, possibly due to elevated isotropic temperatures. The initial degradation temperature (IDT), 50% decomposition temperature and the final decomposition temperature (FDT) are given in the **Table 4.2**. Among these compounds, **8a** exhibited the highest initial thermal decomposition temperature at 378°C, while **8l** had the lowest IDT at 341°C. This suggests that the likelihood of thermal decomposition occurring until this temperature range was low, as depicted in **Figure 4.6**. The 50 % decomposition for all the analysed derivatives occurred in the range 402 to 425°C and the decomposition process was completed in the range of 659 to 753°C.

Table 4.2: TGA thermograms decomposition temperatures for compounds **8a**, **8c**, **8d**, **8g**, **8h**, **8j** and **8l**

Sample Code	IDT (°C)	50% DT (°C)	FDT (°C)
8a	378	423	698
8c	371	422	734
8d	369	415	726
8g	343	418	753
8h	345	425	742
8j	346	410	659
8l	341	402	679

IDT = initial degradation temperature, 50% DT = 50 % decomposition temperature, FDT = full decomposition temperature

4.3.4. Structure-mesomorphic property relationship

In **Figure 4.7**, a graphic depiction illustrates the transition temperature as a function of the number of C-atoms in the terminal chain. This figure provides insights into various transition curves, including Cr-mesophase, SmA-N*, SmC*-SmA, and N*/SmA-Iso.

The transition temperatures from N*/SmA to the isotropic phase are plotted on a single curve. Notably, this curve exhibits a distinct odd-even effect, primarily observed within the first five members of the series. The transition points from SmA to N* follow a gradually ascending curve, with the peak occurring at the decyloxy derivative. Conversely, the transition from SmC* to SmA exhibits a declining trend with an increasing terminal chain length. The curve representing the transition from the crystalline phase (Cr) to the initial mesophase rises and reaches its maximum at the hexyloxy derivative where the increasing terminal chain length

is not conductive to the parallel arrangement of the molecule and the liquid crystalline mesophase range becomes narrower. Subsequently, a sharp decline is observed upon entering the enantiotropic SmA mesophase, followed by a resurgence until the decyloxy derivative. However, from the dodecyloxy derivative onwards, a steep decline continues, gradually decreasing until the octadecyl derivatives. In Series I compounds, the nematic-isotropic transition temperature tends to drop with the increasing alkoxy chain length, and the instigation of the smectic mesophase from medieval homologue is also a common trend. In such a system, this particular trend is anticipated [61–63]. The decreasing trend in N*/SmA to the isotropic phase can be attributed to the difference in molecular stiffness and flexibility on the one side of the molecule. In lower homologues, there is least separation between aromatic nuclei and highest terminal cohesions, leading to the formation of purely nematic phases. As we move up the series, the lateral cohesive forces become more pronounced, causing the molecules to arrange themselves in a layered structure before transitioning into the nematic phase.

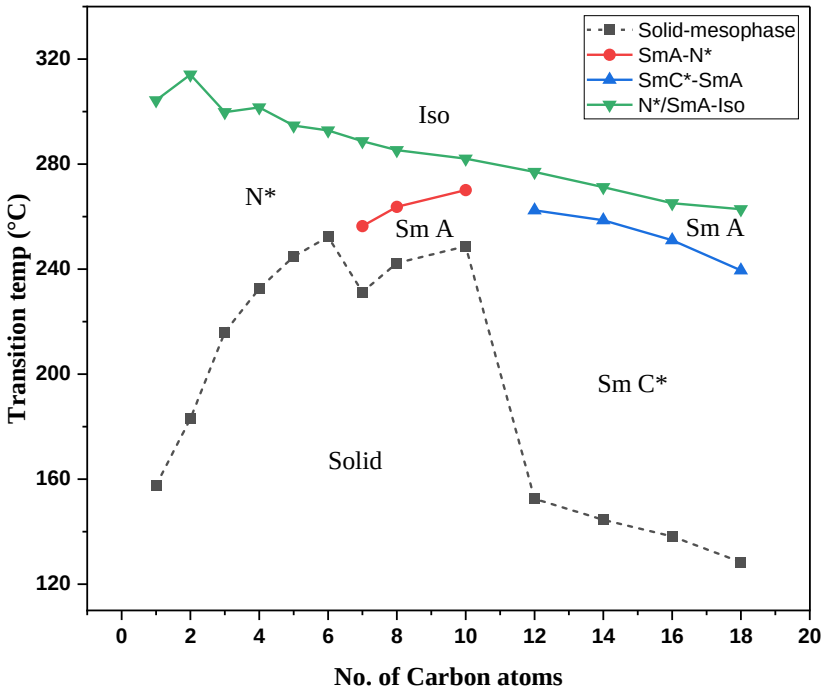

Figure 4.7: Plot of transition temperatures (°C) versus number of carbon atoms in the alkoxy chain

In higher homologues, where intermolecular interactions are relatively weak to preserve equivalent molecular alignment, the prevalence of smectogenic properties is expected to overshadow the stability of the nematic phase as observed.

The liquid crystalline properties of organic compounds have a close relationship with their molecular structure, and these properties, in turn, play a significant role in determining their thermal stability. By examining the molecular composition, a correlation can be

established between the mesogenic properties of these compounds and their thermal stability measurements i.e., N/N*- Iso (for clearing temperatures) and SmA/SmC/SmC*- N/N* (for thermal stability of different phases). **Table 4.3** provides a comparison of the average thermal stabilities among various LC series.

Comparing the molecular structure of the current **Series I** with described series:

(1) 5-(4'-n-alkoxyphenyl)-2-(4"-cholesteryl carbonate)-benzylideneamino-1,3,4-thiadiazoles; **Series I**

(2) "5-(4-n-alkoxyphenyl)-2-(4-n-octyloxy)-benzylideneamino-1,3,4-thiadiazoles"; **Series A** [64]

(3) "5-(4-n-alkoxyphenyl)-2-(4-(2-methylbutoxy))-benzylideneamino-1,3,4-thiadiazoles"; **Series B** [65]

(4) "4,4´-n-alkoxy benzylidene amino cholesteryl carbonate"; **Series C** [40]

The structures of the comparative molecules is given in **Figure 4.8**.

Table 4.3: Average thermal stabilities (°C) of Series I, A, B and C compounds.

Series	**I**	**A**	**B**	**C**
N/N*- Iso	288.7	204.9	164.3	278.5
	($C_{5\text{-}8,10}$)	($C_{5\text{-}10}$)	($C_{4\text{-}10}$)	($C_{5\text{-}8,10}$)
SmA/SmC/SmC*-	263.4	192.7	145.7	259.6
N/N*	($C_{7,8,10}$)	($C_{7\text{-}10}$)	($C_{7\text{-}10}$)	($C_{7,8,10}$)

The compounds of Series I consist of the formyl phenyl cholesteryl carbonate moiety linked to 5-(4'-n-alkoxyphenyl)-2-amino-1,3,4-thiadiazole, forming an imine linkage, while in Series A the 4-n-octyloxybenzaldehyde is linked to 5-(4'-n-alkoxyphenyl)-2-amino-1,3,4-thiadiazole to form Schiff's base linkage. The higher N*- Iso thermal stability of Series I can be attributed to the cholesterol moiety as compared to the long alkyl chain in Series A.

Cholesterol is a rigid, planar and highly structured molecule with multiple rings which allows cholesterol molecules to pack closely together in a solid state, leading to stronger intermolecular forces. These strong intermolecular forces require more energy to break, resulting in a higher melting point. In contrast, alkyl chain derivatives have relatively simple, linear structures. These molecules do not have the ability to form strong intermolecular forces, which results in lower melting points. Furthermore, in SmA/SmC/SmC* - N/N* transition the presence of a cholesterol moiety increases the stability of the nematic phase by introducing chirality and forming a helical structure which helps maintain the alignment of liquid crystal molecules and minimizes disruptive thermal fluctuations. The presence of chirality in Series I

leads to the formation of a chiral nematic (cholesteric) mesophase, which exhibits unique optical properties due to the helical arrangement of molecules as compared to nematic mesophase in Series A with aligned but non-twisted molecules.

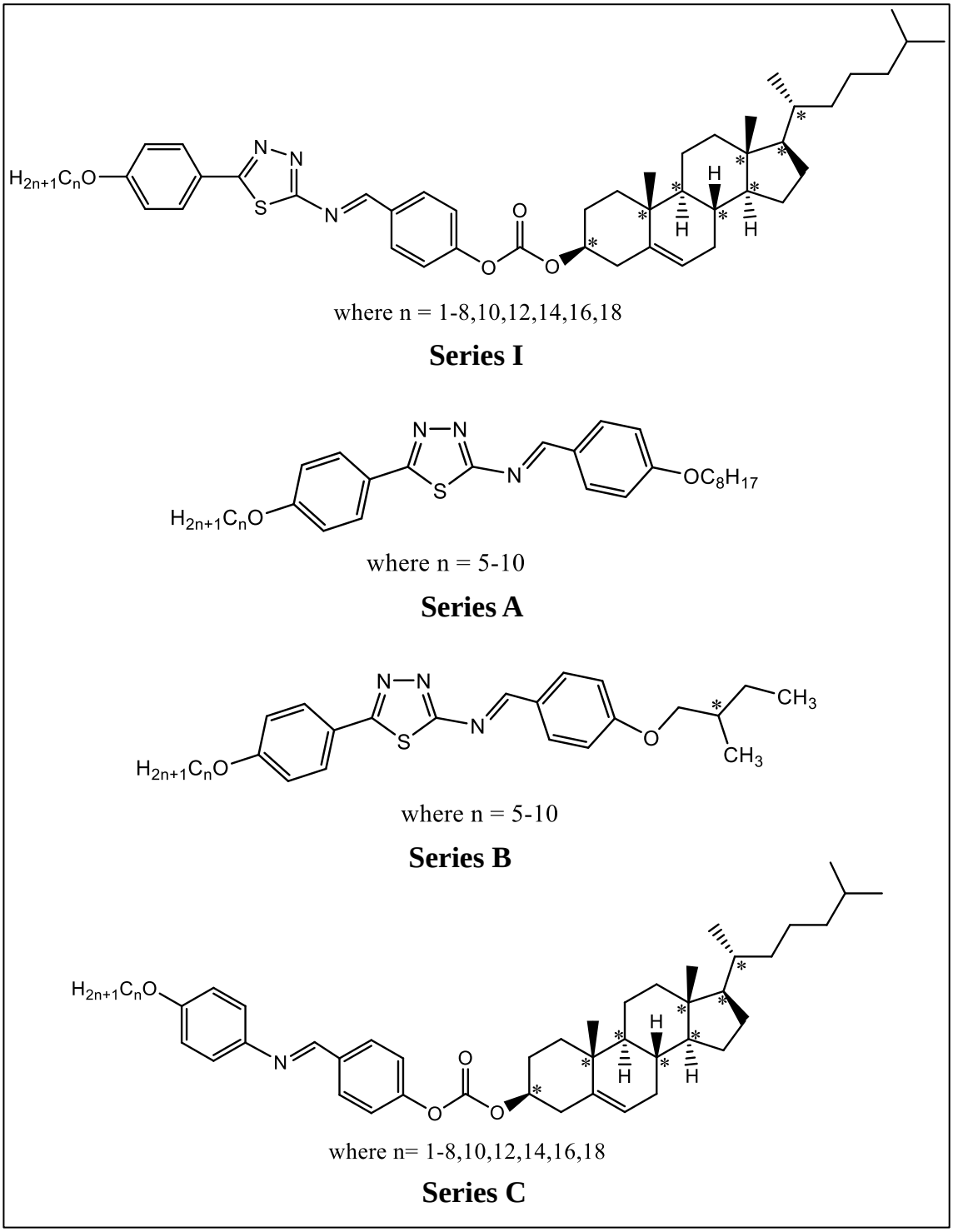

Figure 4.8: The geometric comparison of **Series I, A, B** and **C**

In Series B, cholesteryl carbonate group in Series I has been substituted with a chiral 2-methylbutoxy group. This chiral element, results in the emergence of a chiral nematic mesophase within Series B. As discussed above the higher mesophase stability of Series I as compared to the Series B is due to the rigid and bulky chiral cholesterol group which introduce steric hindrance, making it difficult for molecules to move out of their ordered positions as compared to the small chiral 2-methylbutoxy group.

In Series C, the 5-(4'-n-alkoxyphenyl)-2-amino-1,3,4-thiadiazole of Series I has been replaced with 4-n-alkoxy anilines. With the introduction of 1,3,4-thiadiaole core results in increase in thermal stability of both N*- Iso and SmA/SmC/SmC* - N/N* transition compared to Series C. However, the surge in stability is not particularly substantial.

The instigation of the smectic mesophase from lower members in Series A as well as Series B is because of the alkyl chains' flexibility, which allows for layer formation, favouring the smectic phase, while in Series I cholesterol's rigid, planar structure tends to align the molecules in a particular direction, favouring the nematic phase. As evident from **Table 3**, Series A exhibits greater thermal stability compared to Series B. This difference can likely be attributed to the presence of a methyl branch in the chiral group within Series A which introduces an additional deviation from linearity, disrupting the formation of stable mesophases. This demonstrates how even slight changes in chemical structure can adversely affect a compound's thermal and mesophase stability.

4.3.5. Radical-scavenging activity of mesogens

In vitro radical scavenging activities of the synthesised mesogens were evaluated according to a reported method [66]. The percentage inhibition of the synthesised compounds against DPPH was calculated using.

$$\% \text{ Inhibition} = [(A_{control} - A_{sample}) / A_{control}] \times 100$$

where $A_{control}$ = abs. of control, A_{sample} = abs. of test compounds.

The antioxidant activity is reported as a percentage of inhibition and an IC_{50} (effective concentration for scavenging 50% of the initial DPPH). It was compared with the standard ascorbic acid.

The results obtained in **Table 4.4** indicate that all the synthesised mesogenic derivatives exhibited a comparable degree of radical scavenging activity against the DPPH radical, with the highest activity for compound **8f** with IC_{50} value of 58.05 as compared to the standard ascorbic acid having IC_{50} value of 55.82.

Table 4.4: Radical-scavenging activity of mesogens: % inhibition and IC_{50} values of the DPPH free radical scavenging assay

Sample code	% Inhibition[a]			IC 50(µg/ml)
	50 µg/ml	100µg/ml	200µg/ml	
8a	39.04 ± 0.74	59.05 ± 0.56	70.75 ± 0.04	84.94
8b	43.60 ± 0.61	51.43 ± 0.07	68.07 ± 0.97	89.97
8c	31.48 ± 0.04	54.68 ± 0.64	60.76 ± 0.68	122.5
8d	30.34 ± 0.41	60.72 ± 0.53	65.14 ± 0.48	106.57
8e	41.20 ± 0.85	62.9 ± 0.24	69.1 ± 0.24	70.7
8f	44.60 ± 0.90	65.3 ± 0.04	82.47 ± 0.96	58.05
8g	35.55 ± 0.63	63.8 ± 0.39	76.71 ± 0.29	82.43
8h	40.76 ± 0.01	56.23 ± 0.27	73.07 ± 0.78	84.61
8i	42.96 ± 0.12	62.08 ± 0.98	80.41 ± 0.31	67.46
8j	38.10 ± 0.85	50.7 ± 0.26	69.06 ± 0.85	103.79
8k	33.30 ± 0.12	55.16 ± 0.67	57.48 ± 0.18	126.21
8l	31.88 ± 0.08	51.44 ± 0.92	58.63 ± 0.24	133.13
8m	29.60 ± 0.42	48.93 ± 0.01	54.5 ± 0.19	154.36
STD[b]	45.64 ± 0.03	67.13 ± 0.03	91.78 ± 0.37	55.821
Blank[c]	-	-	-	-

[a] Values represent the mean ± standard error mean (SEM) of three experiments.

[b] Ascorbic acid used as standard

[c] No inhibition

4.3.6. Optical Properties

The UV-Visible absorption spectra for compounds **8a-m**, dissolved in $CHCl_3$ solution, are depicted in **Figure 4.9**. **Table 4.5** provides the photophysical data associated with these compounds. Owing to their structural resemblance, the absorption spectra of compounds **8a-m** were all quite similar in shapes. In the absorbance spectra, all compounds displayed λ_{max} at approximately 374 nm, aligning with their highest absorption peaks. The band at higher energy (259 nm) is due to π-π* electronic transitions of the phenyl ring, while the band at lower energy (374 nm) is due to n- π* transition of the imine linkage (CH=N) [67,68]. It was observed that the chain length did not have much effect on the optical properties. The absorbance was found to be maximum for the compound **8l** and for compound **8e** absorbance was minimum.

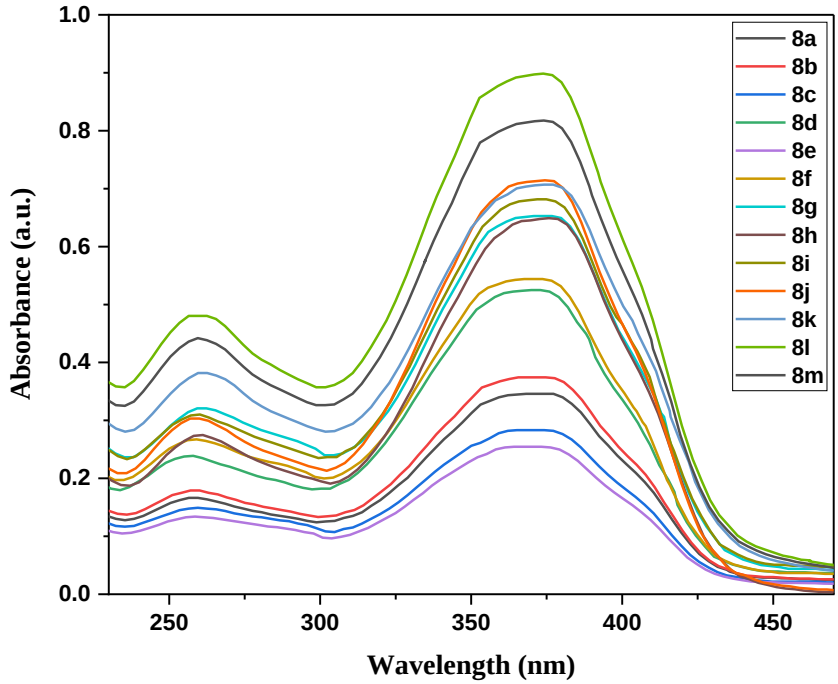

Figure 4.9: UV absorbance spectra of compounds **8a-m**

Liquid crystalline materials with photoluminescent properties have been utilized in a range of applications [69]. The combination of photoluminescence and cholesteric liquid crystal provides interesting complementary features for optimized display applications [70].

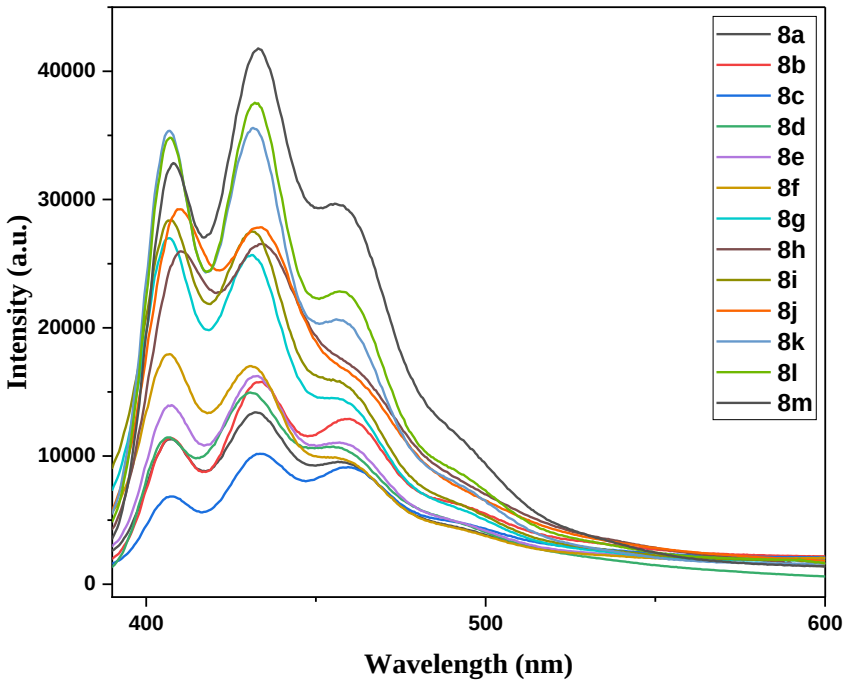

Figure 4.10: Fluorescence spectra of compounds **8a-m** in chloroform ($1x10^{-5}$M). All of the compound were excited at 375 nm

Table 4.5: UV and fluorescence peaks for compounds **8a-m.**

Compounds	UV (nm)	Fluorescence (nm)[a]	Stokes shift (nm)	Φ_{PL}[b]
8a	259,374	407,432,457	33	0.23
8b	260,374	407,434,460	33	0.25
8c	259,374	407,433,459	33	0.20
8d	257,372	406,431,456	34	0.25
8e	258,373	407,433,457	34	0.28
8f	259,373	407,431,456	34	0.30
8g	259,375	407,431,456	32	0.36
8h	261,375	409,434,457	34	0.39
8i	260,374	407,432,457	33	0.39
8j	257,374	409,434,456	35	0.41
8k	259,374	406,431,456	32	0.45
8l	259,373	407,432,457	34	0.46
8m	259,374	408,433,456	34	0.48

[a]Excited at 375 nm.

[b]Determined using quinine sulphate as standard (Φ_{PL} = 0.546 in 1N H_2SO_4).

In order to assess the link between structures and their photophysical properties, the photoluminescence spectra of synthesised compounds were carried out in $CHCl_3$ ($1x10^{-5}$ M) at wavelengths 300-800 nm with an excitation wavelength set to 375 nm. The excitation and emission bandwidths in all the analysis were set to 5 nm. Notably, all the compounds **8a-8m** exhibit pronounced fluorescence at the wavelength 400–480 nm. Compounds when dissolved in solution, showed blue emission, with same luminescent profile characterized by three distinct emission peaks, as graphically depicted in **Figure 4.10**. Comprehensive photophysical data for these compounds are presented in **Table 4.5**. The presence of a 4-n-alkoxy group at the molecule's terminal end, along with a thiadiazole moiety, jointly contribute to an intramolecular charge transfer (ICT) phenomenon in the same direction. The incorporation of a carbonate group and a Schiff's base within the molecules significantly impacts the ICT process, leading to the fluorescence emission spectrum [71]. With the increasing terminal chain length, there is a continuous increase in the fluorescence intensity. The examination of fluorescence quantum yields in $CHCl_3$ (1×10^{-6} M) solution shows that all the compounds show remarkable photoluminescence quantum yield ranging between 0.20 to 0.48 when compared to the standard (quinine sulphate dissolved in 1 N sulfuric acid; Φ_{PL} = 0.546),

suggesting their strong fluorescence efficiency. This not only reveals their distinct molecular dynamics but also points towards their significant potential in applications related to optoelectronics and photonics. The higher homologues in the series lead to a stronger emission resulting in higher fluorescence quantum yield. The stokes shifts displayed by all compounds are almost identical, ranging from 32 to 35 nm.

In conclusion, the photoluminescence spectra of all the synthesised compounds exhibit emission in the blue region (400–480 nm), indicating that all of the compounds have blue light emission properties that can be utilised in potential applications in light-emitting diodes, light-emitting electrochemical cells (LECs), bio-sensing, chemical-sensing, optical-sensing and many more [72–74].

4.3.7. DFT studies

4.3.7.1. Optimized Molecular Structures and HOMO-LUMO energies

A comprehensive analysis was conducted utilizing Density Functional Theory (DFT) to get a deeper insight into the molecular conformation, molecular orbitals and electrostatic potential distribution (ESP), of the thiadiazole derivatives. Complete geometry optimizations were performed without any constraints using the Gaussian 09, revision A.02 software application package [75]. DFT calculations were performed utilizing the "Becke3–Lee–Yang–Parr hybrid functional" (B3LYP) for exchange–correlation and the 6-31G (d, p) basis set. Stability of all the compounds was established by the optimized structure inside the system, as evidenced by the lack of any possible imaginary frequencies **(Figure 4.11)**.

(Figure 4.11) clearly illustrated molecular structures, with atoms color-coded as: grey for carbon (C), blue for nitrogen (N), red for oxygen (O), and white for hydrogen (H). The atoms were linked together using sigma and pi bonds to create a 3-D model of the molecules. **(Figure 4.11)** displays the most effective molecular configuration observed for thiadiazole cholesterol derivatives. **Table 4.6** presents the optimized energies for specific derivatives, while **Figure 4.12** illustrates the correlation between the number of carbon atoms in the terminal chain of synthesized compounds and the energy minima in Hartree units. The graph indicates that with an increase in the number of carbon atoms in the terminal chain, there is a corresponding decrease in the energy minima, indicating greater stability in the molecular structure. This suggests that longer chains result in more energetically favorable

conformations, possibly due to improved flexibility and conformational freedom in the molecule.

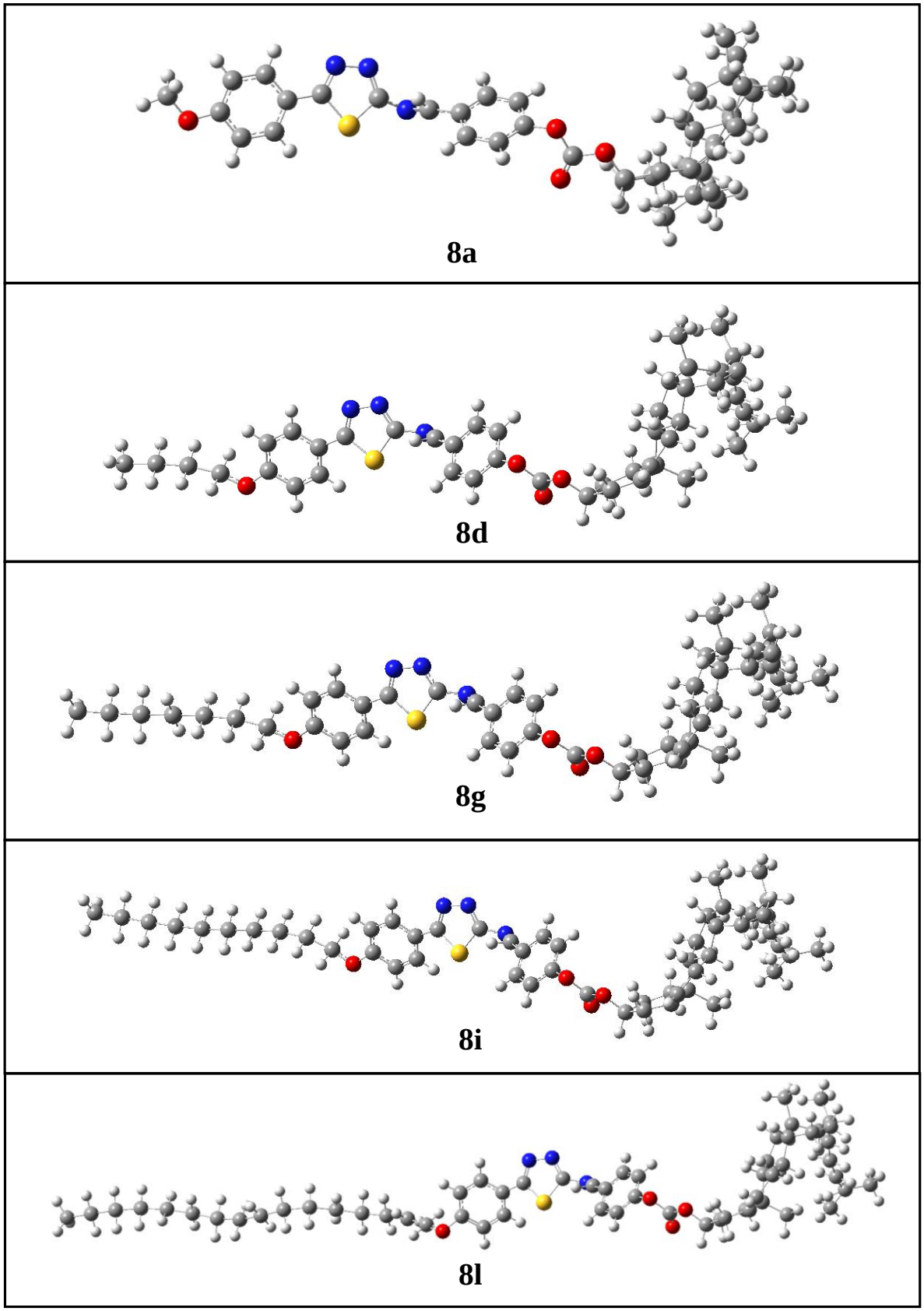

Figure 4.11: Optimized molecular structures of thiadiazole cholesterol derivatives

Table 4.6: Optimized energy (in Hartree)

Sample	Energy Minima (Hartree)
8a	-2572.145
8d	-2689.572
8g	-2806.664
8i	-2924.009
8l	-3158.621

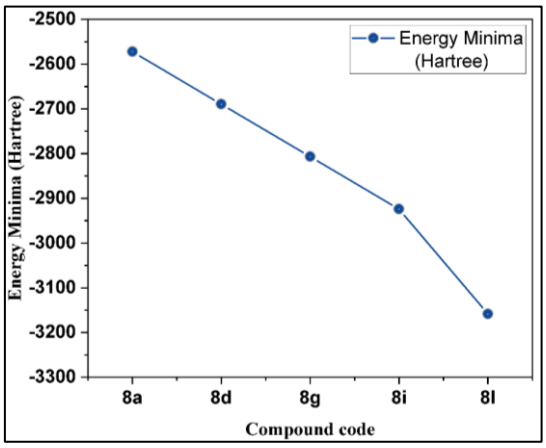

Figure 4.12: Dependence of the terminal alkoxy chain on the energy minima

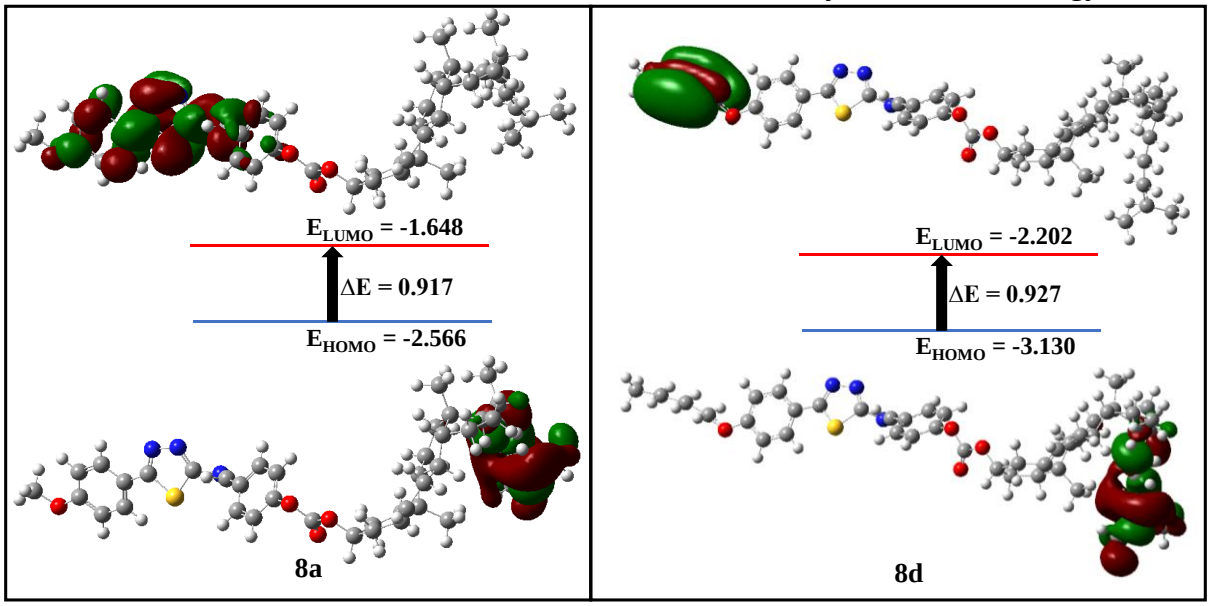

Figure 4.13 (a): FMO contours of structures **8a** and **8d**

An accurate description of the HOMO and LUMO, detailing their absolute energy, atomic orbital composition, as well as relative energy gap, offers important insights into the photo-physical characteristics necessary for the development of new molecules and modifying specific properties of compounds. The calculated HOMO and LUMO energies are shown in **Table 4.7**, and 3D iso-surface maps of these orbitals for the compounds can be found in **Figure 4.13 (a-c)**. The electron density of the orbitals in the HOMO was mostly concentrated over the iso-octyl side chain of the cholesterol molecule, except for 8l, where it was observed over the terminal alkoxy chain. Conversely, the electron density of the orbitals in the LUMO was mainly concentrated over the terminal alkoxy chain. Electron density for LUMO in **8a** was observed on the aromatic part of the molecule, including the 1,3,4-thiadiazole aromatic core, and for **8l** LUMO, electron density was focused on the alkoxy chain near the ether linkage and aromatic part.

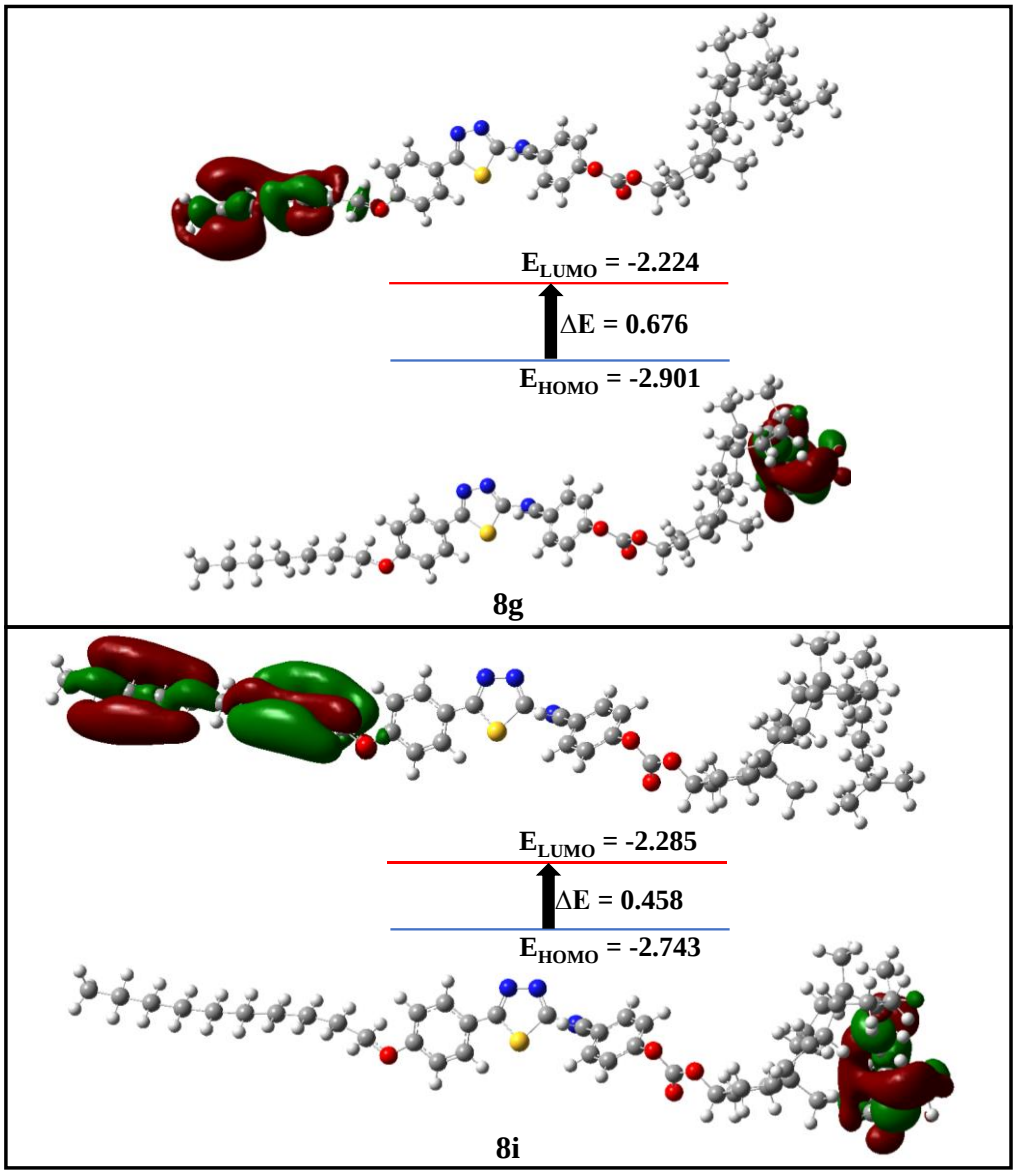

Figure 4.13 (b): FMO contours of structures **8g** and **8i**

The difference in energy levels between the HOMO and the LUMO might indicate the kinetic stability of a molecule, providing insights into its reactivity [76,77]. A large HOMO–LUMO gap suggests enhanced kinetic stability and decreased chemical reactivity. Adding electrons to a high-energy LUMO or withdrawing electrons from a low-energy HOMO is energetically not favorable [78]. The energy gap (ΔE) for synthesized thiadiazole derivatives was obtained in the range of 0.251–0.917. A smaller energy gap in the FMO increases the probability of the molecule participating in electronic transitions and chemical reactions. This indicates a greater reactivity of the molecule, which might result in enhanced electrical conductivity or fluorescence properties. This also confirms the increased fluorescent intensity with increasing terminal chain length as discussed in section **4.3.6**. Analysis from **Table 4.7** revealed a decrease in mesogen reactivity, following the order: **8a < 8d < 8g < 8i < 8l**.

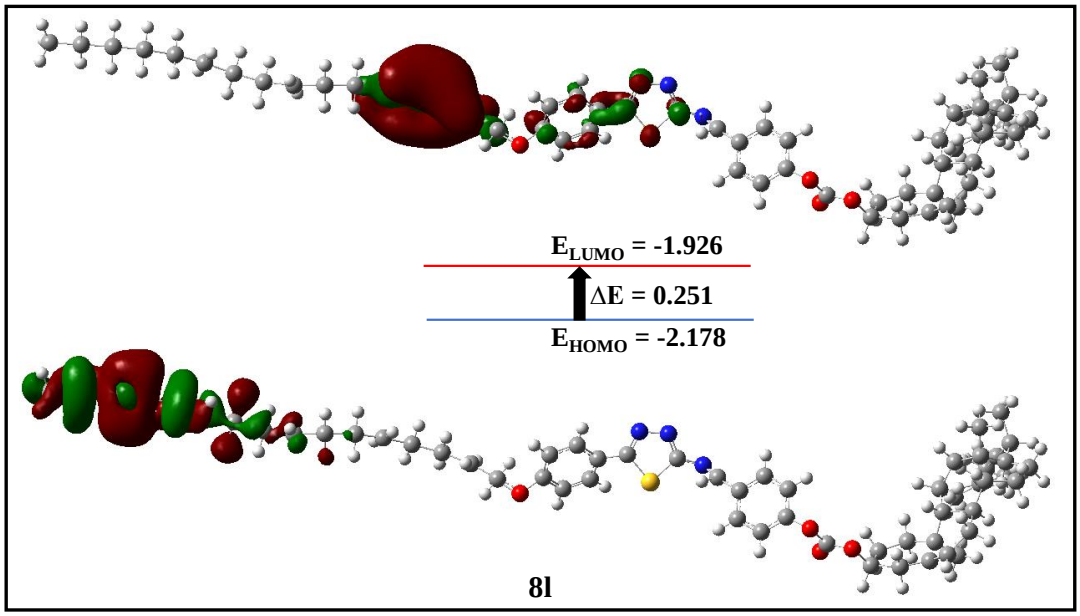

Figure 4.13 (c): FMO contours of structure **8l**

Table 4.7: Calculated molecular properties of the cholesterol compounds using DFT

Sample	E_{HOMO} (eV)	E_{LUMO} (eV)	ΔE (eV)	η Global hardness	δ = 1/η Global softness	μ_{el} (eV)	ω Electrophilicity index
8a	-2.566	-1.648	0.917	0.45	2.17	-2.10	4.83
8d	-3.130	-2.202	0.927	0.46	2.15	-2.66	7.66
8g	-2.901	-2.224	0.676	0.33	2.95	-2.56	9.70
8i	-2.743	-2.285	0.458	0.22	4.36	-2.51	13.80
8l	-2.178	-1.926	0.251	0.12	7.93	-2.05	16.72

Table 4.7 presents the frontier Molecular Orbital (MO) energy and various reactivity parameters for the optimized molecular structures [79]. These parameters include the electronic chemical potential (μ_{el}), chemical hardness (η), and electrophilicity index (ω), which offer valuable insights into the chemical reactivity and stability of the compounds. The compounds exhibited chemical potentials ranging from -2.05 to -2.66 eV and hardness values ranging from 0.12 to 0.46 eV, with the lowest observed for **8l**. Compound **8l** demonstrates higher reactivity compared to the other compounds in the series, indicating its softer nature. Additionally, a trend of increasing electrophilicity is observed in the sequence: **8a** < **8d** < **8g** < **8i** < **8l**, suggesting a decrease in electron density or an increase in electron-withdrawing characteristics among the mesogens. Consequently, **8l** displays heightened reactivity towards electrophiles.

Table 4.8: Dipole moment for cholesterol derivatives

Sample	μ_x	μ_y	μ_z	Dipole Moment μ_{dip} (Debye)
8a	-1.7963	0.8994	-3.3063	3.8688
8d	-3.8900	0.4458	-2.7417	4.7800
8g	-9.1737	1.5275	-4.2281	10.2160
8i	-6.7614	0.7693	-3.8561	7.8217
8l	7.4617	2.0754	-5.8763	9.7219

Dipole moments have been calculated for the selected compounds in three Cartesian axis **(Table 4.8)**. The high dipole moments indicate the mesogenic properties of the compounds. Differences in molecular polarity among the samples are reflected in their varying dipole moments. Compounds with higher dipole moments, like **8g** and **8l**, are expected to exhibit more polarized molecules, whereas those with lower dipole moments, such as **8a** and **8d**, are comparatively less polar. These variations in dipole moments play a crucial role in determining liquid crystal behaviour, affecting factors like phase transitions and optical properties. Higher dipole moments may enhance electro-optical responses or modify phase transition temperatures.

4.3.7.2. Molecular Electrostatic Potential (MEP)

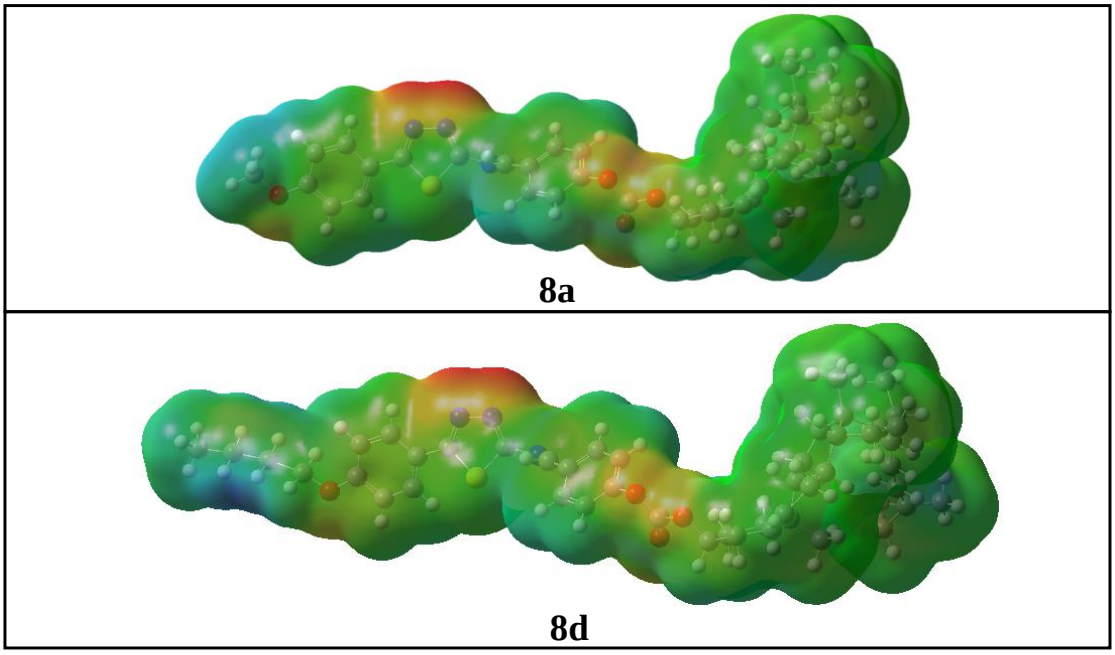

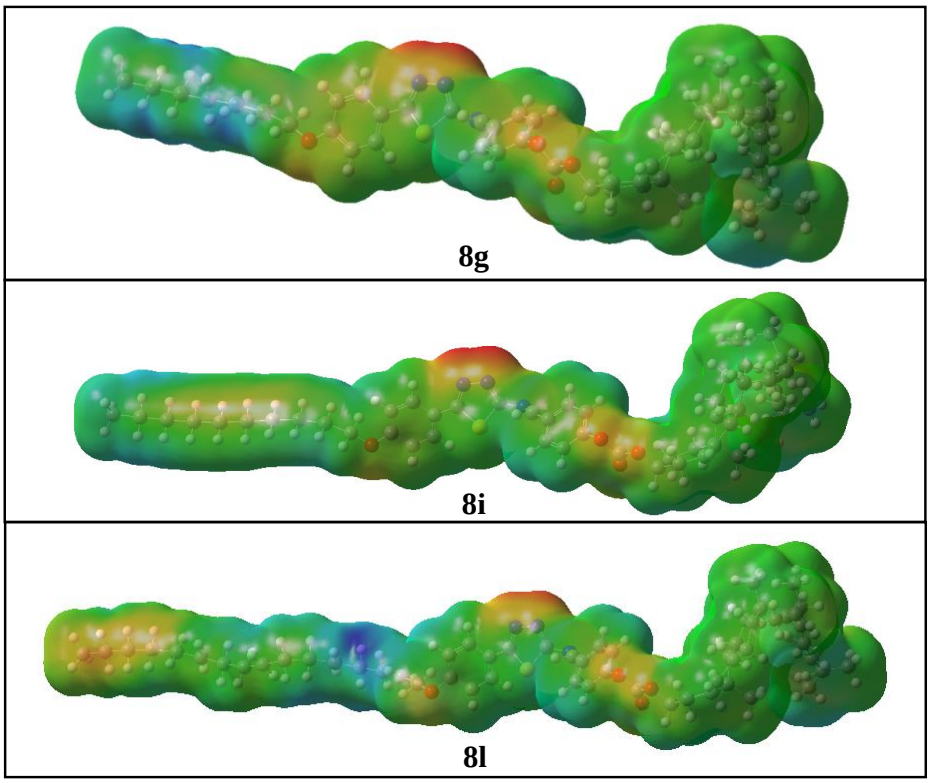

Figure 4.14: MEP mapping of some thiadiazole cholesterol derivatives

The charge distribution map for the synthesized thiadiazole derivatives was determined using the B3LYP-6-31 G basis sets via molecular electrostatic potential (MEP) calculations **(Figure 4.14)**. The MEP analysis is typically conducted to anticipate potential reactive sites within a molecule, indicating where electrophilic or nucleophilic attacks might occur. Additionally, it provides insights into the electrostatic potential (ESP) and charge distribution within the molecule, essential for examining its interactions with other molecules. In the MEP surface visualization, blue typically indicates areas of electronic charge depletion with higher potential, while red signifies regions of lower potential where electronic charge accumulates. Lower potential regions are preferable for electrophilic attacks, while higher potential regions are conducive to nucleophilic attacks. The ESP of the MEP surface follows the trend: red < orange < yellow < green < blue. The MEP map indicates that the N-N bond within the thiadiazole ring and the carbonate group exhibit a lower ESP energy surface, allowing for electronic charge accessibility.

4.4. Conclusion

In conclusion, we have successfully designed and synthesised thirteen new homologues by condensing 4-formyl phenyl cholesteryl carbonate with 5-(4'-n-alkoxyphenyl)-2-amino-

1,3,4-thiadiazole, exhibiting multiple mesophases including chiral nematic (N*), twist grain boundary-A (TGB_A), smectic A (SmA), and chiral smectic C (SmC*) phases. In the plot of transition temperature versus number of carbon atoms in the alkoxy chain, the smectic A to chiral nematic curve rises to maximum with the increasing terminal chain length, while smectic C* to smectic A shows a falling tendency. The chiral nematic/smectic A to isotropic transition shows a usual falling tendency. Some of the mesogens showed good to moderate radical scavenging activity. Also, all the compounds are UV-active and show photoluminescence in the blue emission region. As the terminal chain length increases, more pronounced emission and the higher fluorescence quantum yield was observed. This was also discussed from the DFT studies where the lower energy gap in FMO suggests better fluorescence emission. DFT calculations were additionally conducted to provide insights into theoretical chemical reactivity, encompassing analysis of Frontier MOs and MEP mapping. These calculations involved measuring energy gaps and identifying regions of both low and high electron density.

4.5. References

[1] CROCKETT EL. Cholesterol Function in Plasma Membranes from Ectotherms: Membrane-Specific Roles in Adaptation to Temperature1. Amer Zool. 1998;**38**:291–304.

[2] Shinkai S, Murata K. Cholesterol-based functional tectons as versatile building-blocks for liquid crystals, organic gels and monolayers. J Mater Chem. 1998;**8**:485–495.

[3] Yelamaggad CV, Shanker G, Hiremath US, et al. Cholesterol-based nonsymmetric liquid crystal dimers: an overview. J Mater Chem. 2008;**18**:2927–2949.

[4] Yelamaggad CV, Nagamani SA, Hiremath US, et al. Cholesterol-based dimeric liquid crystals: synthesis and mesomorphic behaviour. Liq Cryst. 2001;**28**:1009–1015.

[5] Galatina AI, Novikova NS, Derkach LG, et al. Structure and Mesomorphism of Cholesteric Liquid Crystals. Molecular Crystals and Liquid Crystals. 1986;**140**:11–81.

[6] Harwood SM, Toyne KJ, Goodby JW, et al. The synthesis of cholest-5-ene-3beta-carboxylates and a comparison of their mesomorphic behaviour with isomeric cholesterol esters with a reversed ester linkage. Liquid Crystals. 2000;**27**:443–449.

[7] Shubashree S, Sadashiva BK. Twist grain boundary smectic A phase in compounds derived from cholesterol. Current Science. 2003;**85**:1061–1065.

[8] Shubashree S, Sadashiva BK. Synthesis and mesomorphic properties of compounds exhibiting the undulated twist grain boundary smectic C* phase. Liquid Crystals. 2004;**31**:81–89.

[9] Chen R, Wang L, An Z, et al. Effect of π-conjugation units on the liquid crystal and photovoltaic performance of heterocyclic pyridine-based compounds. Liq Cryst. 2021;**48**:2178–2187.

[10] Zhang H, Shiino S, Shishido A, et al. A Thiophene Liquid Crystal as a Novel π-Conjugated Dye for Photo-Manipulation of Molecular Alignment. Adv Mater. 2000;**12**:1336–1339.

[11] Hutchison GR, Ratner MA, Marks TJ. Intermolecular Charge Transfer between Heterocyclic Oligomers. Effects of Heteroatom and Molecular Packing on Hopping Transport in Organic Semiconductors. J Am Chem Soc. 2005;**127**:16866–16881.

[12] Park YS, Kim D, Lee H, et al. Donor-acceptor-donor-type liquid crystal with a pyridazine core. Org Lett. 2006;**8**:4699–4702.

[13] O'Neill M, Kelly S m. Liquid Crystals for Charge Transport, Luminescence, and Photonics. Adv Mater. 2003;**15**:1135–1146.

[14] Seed AJ, Hird M, Styring P, et al. Heterocyclic Esters Exhibiting Frustrated Liquid Crystal Phases. Mol Cryst Liq Cryst Sci Technol Sec A Mol Cryst Liq Cryst. 1997;**299**:19–25.

[15] Barbarella G, Zambianchi M, Pudova O, et al. Oligothiophene Isothiocyanates as a New Class of Fluorescent Markers for Biopolymers. J Am Chem Soc. 2001;**123**:11600–11607.

[16] Su S-J, Cai C, Kido J. RGB Phosphorescent Organic Light-Emitting Diodes by Using Host Materials with Heterocyclic Cores: Effect of Nitrogen Atom Orientations. Chem Mater. 2011;**23**:274–284.

[17] Feng Z, Cheng Z, Jin H, et al. Recent progress of sulphur-containing high-efficiency organic light-emitting diodes (OLEDs). J Mater Chem C. 2022;**10**:4497–4520.

[18] Parra ML, Elgueta EY, Ulloa JA, et al. Columnar liquid crystals based on amino-1,3,4-thiadiazole derivatives. Liq Cryst. 2012;**39**:917–925.

[19] Han J, Wang J, Zhang F, et al. Synthesis and mesomorphic behaviour of heterocycle-based liquid crystals containing 1,3,4-oxadiazole/thiadiazole and thiophene units. Liq Cryst. 2008;**35**:1205–1214.

[20] Seltmann J, Marini A, Mennucci B, et al. Nonsymmetric bent-core liquid crystals based on a 1,3,4-thiadiazole core unit and their nematic mesomorphism. Chem Mater. 2011;**23**:2630–2636.

[21] Tuzimoto P, Santos DMPO, Moreira T dos S, et al. Luminescent liquid crystals containing a sulphur-based heterocyclic core. Liq Cryst. 2014;**41**:1097–1108.

[22] Tomi IHR, Al-Heetimi DTA, Jaffer HJ. Asymmetric 1,3,4-thiadiazole derivatives: Synthesis, characterization and studying their liquid crystalline properties. J Mol Struct. 2017;**1141**:176–185.

[23] Dimitrowa K, Hauschild J, Zaschke H, et al. Kristallin-flüssige 1,3,4-Thiadiazole. I. Biphenyl- und terphenylanaloge 1,3,4-Thiadiazole. J Prakt Chem. 1980;**322**:933–944.

[24] Han J, Wang Q, Wu J, et al. Synthesis and liquid crystalline property of H-shaped 1,3,4-thiadiazole dimers. Liq Cryst. 2015;**42**:127–133.

[25] Zhong W-Y, Song L-Q, Zhou B, et al. Synthesis, mesomorphic and fluorescent properties of 1,3,4-oxadiazoles/thiadiazoles with a terminal 3-fluoro-4-cyanophenyl group. Tetrahedron. 2023;**144**:133579.

[26] Saha SK, Deb J, Sarkar U, et al. Hockey-stick-shaped mesogens based on 1,3,4-thiadiazole: synthesis, mesomorphism, photophysical and DFT studies. Liq Cryst. 2017;**44**:2203–2221.

[27] He CF, Richards GJ, Kelly SM, et al. Heterocyclic polycatenar liquid crystals. Liquid Crystals. 2007;**34**:1249–1267.

[28] Saha SK, Mohiuddin G, Paul MK, et al. Polar Switching and Cybotactic Nematic Ordering in 1,3,4-Thiadiazole-Based Short-Core Hockey Stick-Shaped Fluorescent Liquid Crystals. ACS Omega. 2019;**4**:7711–7722.

[29] Al-Malki MKS, Hameed AS, Al-Dujaili AH. Synthesis and Mesomorphic Properties of New Columnar Liquid Crystal Containing 1,3,5-triiminebenzene with Pendant 1,3,4-thiadiazole Group. Mol Cryst Liq Cryst. 2014;**593**:34–42.

[30] Olate FA, Parra ML, Vergara JM, et al. Star-shaped molecules as functional materials based on 1,3,5-benzenetriesters with pendant 1,3,4-thiadiazole groups: liquid crystals, optical, solvatofluorochromic and electrochemical properties. Liquid Crystals. 2017;**44**:1173–1184.

[31] Elgueta EY, Parra ML, Barberá J, et al. New polycatenar Schiff bases derived from 1,3,4-thiadiazole: synthesis, mesomorphism and luminescence behaviour. Liq Cryst. 2016;**43**:1649–1658.

[32] Tandel RC, Patel NK. Synthesis and mesomorphic properties of chiral nematic liquid crystals based on cholesterol. Liq Cryst. 2014;**41**:514–521.

[33] Lee H-C, Lu Z, Henderson PA, et al. Cholesteryl-based liquid crystal dimers containing a sulfur–sulfur link in the flexible spacer. Liq Cryst. 2012;**39**:259–268.

[34] Frizon TEA, Vieira AA, Giacomelli FC, et al. Synthesis of cholesterol containing unsymmetrical dimers: a new series of liquid crystals. Liq Cryst. 2022;**49**:758–768.

[35] Chan T-N, Lu Z, Yam W-S, et al. Non-symmetric liquid crystal dimers containing an isoflavone moiety. Liquid Crystals. 2012;**39**:393–402.

[36] Donaldson T, Staesche H, Lu ZB, et al. Symmetric and non-symmetric chiral liquid crystal dimers. Liq Cryst. 2010;**37**:1097–1110.

[37] Donaldson T, Henderson PA, Achard MF, et al. Non-symmetric chiral liquid crystal trimers. Liquid Crystals. 2011;**38**:1331–1339.

[38] Donaldson T, Henderson PA, Achard MF, et al. Chiral liquid crystal tetramers. J Mater Chem. 2011;**21**:10935–10941.

[39] Hamley IW, Castelletto V, Parras P, et al. Ordering on multiple lengthscales in a series of side group liquid crystal block copolymers containing a cholesteryl-based mesogen. Soft Matter. 2005;**1**:355–363.

[40] Bairwa SK, Sonera SA, Tandel RC. Cholesterol based mesogenic Schiff's base derivatives with carbonate linkage: Synthesis, characterisation and photoluminescence study. Liquid Crystals. 2023;**50**:2495-2509.

[41] Majumdar KC, Shyam PK, Rao DSS, et al. Occurrence of unusually wide thermal range enantiotropic twist grain boundary TGBC* phases in unsymmetrical cholesterol and oxadiazole based liquid crystalline dimers. J Mater Chem. 2010;**21**:556–561.

[42] Pradhan B, Chakraborty N, Gupta RK, et al. Nonsymmetrical cholesterol dimers constituting regioisomeric oxadiazole and thiadiazole cores: an investigation of the structure–property correlation. New J Chem. 2017;**41**:879–888.

[43] Majumdar KC, Mondal S, Ghosh T. Synthesis and Mesomorphic Behavior of Novel Liquid-Crystalline Thiophene Derivatives. Molecular Crystals and Liquid Crystals. 2010;**524**:17–25.

[44] Majumdar KC, Ghosh T, Chakravorty S, et al. Cholesterol-based unsymmetrical Schiff's base dimer terminated with 4-alkoxy-5-phenylthiophene unit: synthesis and characterisation. Liquid Crystals. 2010;**37**:1539–1547.

[45] Jamain Z, Khairuddean M, Guan-Seng T. Synthesis of novel liquid crystalline and fire retardant molecules based on six-armed cyclotriphosphazene core containing Schiff base and amide linking units. RSC Adv. 2020;**10**:28918–28934.

[46] Upadhyay P. K., Mishra P. SYNTHESIS, ANTIMICROBIAL AND ANTICANCER ACTIVITIES OF 5-(4-SUBSTITUTED-PHENYL)-1,3,4- THIADIAZOLE-2-AMINES. Rasayan J Chem. 2017;**10**:254–262.

[47] S.L. Vasoya, D.J. Paghdar, P.T. Chovatia, et al. Synthesis of some New Thiosemicarbazide and 1,3,4-Thiadiazole Heterocycles Bearing Benzo[b]Thiophene Nucleus as a Potent Antitubercular and Antimicrobial Agents. J Sci I R Iran. 2005;**16**:33–36.

[48] Aouad MR, Messali M, Rezki N, et al. Synthesis and characterization of some novel 1,2,4-triazoles, 1,3,4-thiadiazoles and Schiff bases incorporating imidazole moiety as potential antimicrobial agents. Acta Pharm. 2015;**65**:117–132.

[49] Tandel RC, Patel NK. Synthesis and study of liquid crystalline properties of schiff's bases having 1,3,4-thiadiazole moiety. Liq Cryst. 2014;**41**:495–502.

[50] Dierking I, Gießelmann F, Zugenmaier P, et al. Investigations of the structure of a cholesteric phase with a temperature induced helix inversion and of the succeeding Sc* phase in thin liquid crystal cells. Liquid Crystals. 1993;**13**:45–55.

[51] Shanker G, V. Yelamaggad C. Synthesis and Phase Transitional Behavior of Dimer-like Optically Active Liquid Crystals. J Phys Chem B. 2011;**115**:10849–10859.

[52] Zhan X, Jing X, Wu C. Synthesis and mesomorphic properties of a novel series of cholesterol-based liquid crystalline tetramers. Liq Cryst. 2009;**36**:1349–1354.

[53] Dierking I, Gießelmann F, Zugenmaier P. TGB A∗ state in a homologous series of diarylethane α-chloroester ferroelectric liquid crystals. Liquid Crystals. 1994;**17**:17–22.

[54] Prasad SK, Nair GG, Chandrasekhar S, et al. Pressure Induced Twist Grain Boundary Phase. Mol Cryst Liq Cryst Sci Technol Sec A Mol Cryst Liq Cryst. 1995;**260**:387–394.

[55] DIERKING I. A review of textures of the TGBA* phase under different anchoring geometries. Liq Cryst. 1999;**26**:83–95.

[56] Bhat S V, Raghunathan VA, Kumar S. Synthesis and mesomorphic characterization of some novel steroidal mesogens: A structure–property correlation. J Mol Liq. 2021;**340**:117219.

[57] Dierking I. The SmC* Subphases. Textures of Liquid Crystals [Internet]. John Wiley & Sons, Ltd; 2003. p. 123–134. Available from: https://onlinelibrary.wiley.com/doi/abs/10.1002/3527602054.ch8.

[58] Amponsah-Efah KK, Glorieux C, Thoen J, et al. Effect of glycerol on the order of the mesophase transitions of supercooled itraconazole. J Mol Liq. 2020;**320**:114222.

[59] Tan X, Zhang R, Guo C, et al. Amphotropic azobenzene derivatives with oligooxyethylene and glycerol based polar groups. J Mater Chem C. 2015;**3**:11202–11211.

[60] Omar AZ, Alazmi ML, Alsubaie MS, et al. Synthesis of New Liquid-Crystalline Compounds Based on Terminal Benzyloxy Group: Characterization, DFT and Mesomorphic Properties. Molecules. 2023;**28**:3804.

[61] Cruickshank E, Strachan GJ, Majewska MM, et al. The effects of alkylthio chains on the properties of symmetric liquid crystal dimers. New J Chem. 2023;**47**:7356–7368.

[62] Imrie CT, Taylor L. The preparation and properties of low molar mass liquid crystals possessing lateral alkyl chains. Liquid Crystals. 1989;**6**:1–10.

[63] Date RW, Imrie CT, Luckhurst GR, et al. Smectogenic dimeric liquid crystals. The preparation and properties of the α,ω-bis(4- *n* -alkylanilinebenzylidine-4′-oxy)alkanes. Liquid Crystals. 1992;**12**:203–238.

[64] Parra M, Alderete J, Zuńñiga C, et al. Azo compounds and Schiff ’s bases derived from 5-(4-pyridyl)-2-amino-1,3,4-thiadiazole: synthesis, mesomorphic properties and structural study by semi-empirical calculations. Liq Cryst. 2001;**28**:1659–1666.

[65] Xu Y, Li B, Liu H, et al. Liquid crystalline thiadiazole derivatives: new ferroelectric thiadiazole derivatives. Liq Cryst. 2002;**29**:199–202.

[66] Kumar B, Devi J, Manuja A. Synthesis, structure elucidation, antioxidant, antimicrobial, anti-inflammatory and molecular docking studies of transition metal(II) complexes derived from heterocyclic Schiff base ligands. Res Chem Intermed. 2023;**49**:2455–2493.

[67] Sonker E, Tiwari R, Kumar K, et al. Electrical properties of new polyazomethines. SN Appl Sci. 2020;**2**:1123.

[68] Perju E, Marin L. Mesomorphic Behavior of Symmetric Azomethine Dimers Containing Different Chromophore Groups. Molecules. 2021;**26**:2183.

[69] Kumar A, Singh G. Recent advances and future perspectives of photoluminescent liquid crystals and their nanocomposites for emissive displays and other tunable photonic devices. J Mol Liq. 2023;**386**:122607.

[70] Kim J-K, Joo S-H, Song J-K. Complementarity between fluorescence and reflection in photoluminescent cholesteric liquid crystal devices. Opt Express. 2013;**21**:6243–6248.

[71] Goel A, Tomer N, Ghule VD, et al. A multi-responsive pyranone based Schiff base for the selective, sensitive and competent recognition of copper metal ions. Spectrochim Acta - A: Mol Biomol Spectrosc. 2021;**249**:119221.

[72] Yamada S, Uto E, Yoshida K, et al. Development of photoluminescent liquid-crystalline dimers bearing two fluorinated tolane-based luminous mesogens. J Mol Struct. 2022;**363**:119884.

[73] Khan M, Liu S, Qi L, et al. Liquid crystal-based sensors for the detection of biomarkers at the aqueous/LC interface. Trends Analyt Chem. 2021;**144**:116434.

[74] Mohammad A-T, Abbas WR. Liquid crystal behavior, photoluminescence and gas sensing: A new series of ionic liquid crystal imidazole and benzoimidazole bearing chalcone groups, synthesis and characterization. RSC Adv. 2021;**11**:38444–38456.

[75] Frisch M, Trucks G, Schlegel H, et al. Gaussian 09 (Revision A02). Gaussian Inc Wallingford CT. 2009;

[76] Aihara J. Reduced HOMO−LUMO Gap as an Index of Kinetic Stability for Polycyclic Aromatic Hydrocarbons. J Phys Chem A. 1999;**103**:7487–7495.

[77] Aihara J. Correlation found between the HOMO–LUMO energy separation and the chemical reactivity at the most reactive site for isolated-pentagon isomers of fullerenes. Phys Chem Chem Phys. 2000;**2**:3121–3125.

[78] Miar M, Shiroudi A, Pourshamsian K, et al. Theoretical investigations on the HOMO–LUMO gap and global reactivity descriptor studies, natural bond orbital, and nucleus-independent chemical shifts analyses of 3-phenylbenzo[d]thiazole-2(3H)-imine and its para-substituted derivatives: Solvent and substituent effects. Journal of Chemical Research. 2021;**45**:147–158.

[79] Pearson RG. Chemical hardness and the electronic chemical potential. Inorganica Chimica Acta. 1992;**198–200**:781–786.